

Image processing techniques in Magneto-Optic NDT

by

Baoshi Sun

A thesis submitted to the graduate faculty
in partial fulfillment of the requirements for the degree of

MASTER OF SCIENCE

Major: Electrical Engineering

Major Professor: William Lord

Iowa State University

Ames, Iowa

1997

Copyright © Baoshi Sun, 1997. All right reserved.

Graduate College
Iowa State University

This is to certify that the Master's thesis of

Baoshi Sun

has met the thesis requirements of Iowa State University

Signatures have been redacted for privacy

TABLE OF CONTENTS

LIST OF FIGURES	v
LIST OF TABLES	vii
ACKNOWLEDGEMENTS	viii
CHAPTER 1. INTRODUCTION AND NONDESTRUCTIVE TESTING	
METHODS	1
Introduction	1
Methods of Nondestructive Testing	2
Eddy Current Method	3
Multiple Test Frequencies and Data Fusion	4
Ultrasonic Test Method	5
Radiographic Method	6
Microwave Method	6
CHAPTER 2. MAGNETO-OPTIC/EDDY CURRENT IMAGER	7
Introduction and Background	7
Magneto-Optic and Eddy Current Technology	8
Magneto-Optic Sensor	11
Components and Their Properties	11
Garnet Film Response	12
Sheet Current Excitation	13
Linear Sheet Current Excitation	14
Magneto-Optic/Eddy Current Imaging	15
The Forming of The Rivet Image	18
Improvement on MOI-Using Rotating Magnetic Fields	19
Background	19
Multidirectional or Rotating Sheet Current Excitation	20
Frequency and Penetration Depth	21
The Advantages of MOI	22
Imaging Processing Task on Images of MOI	23
CHAPTER 3. CORROSION TYPES AND ALLOYS IN AIRCRAFT	24
Introduction	24
Types and Nature of Corrosion	24
Corrosion Detection Requirements	24
Detection of Hidden Corrosion With the MOI	26
CHAPTER 4. CORRELATION FILTERS FOR TEXTURE RECOGNITION	28
Introduction	28
Derivation of Spatial Filters for Texture Recognition	30

Numerical Computation of the Filter	34
CHAPTER 5. MATHEMATICAL MORPHOLOGY	38
Introduction	38
Binary Morphology	39
Basic Definitions	39
Dilation	39
Erosion	40
Opening and Closing	42
Structuring Elements	45
Decomposition of Structuring Elements	45
Gray Scale Morphology	46
Gray Scale Dilation	47
Gray Scale Erosion	48
Gray Scale Opening and Closing	48
CHAPTER 6. RESULTS AND CONCLUSIONS	51
Introduction	51
Images and Layout	51
Application of Correlation Filter, Averaging, Morphology	55
Correlation Filter	55
Image Averaging	55
Morphological Operations	56
Averaging, Correlation Filter and Morphology Combined Operations	57
Conclusions	61
Future Work	62
BIBLIOGRAPHY	63

LIST OF FIGURES

Figure 1.1: The method of eddy current NDT	3
Figure 2.1: The Magneto-Optic/Eddy Current System.	7
Figure 2.2: The comparison for induction methods between conventional eddy current technique and magneto-optic/eddy current imaging method.	8
Figure 2.3: The Faraday Magneto-Optic effect.	10
Figure 2.4: The Magneto-Optic/Eddy Current Imager uses a reflection mode geometry, this doubles the effective rotation angle.	10
Figure 2.5: How the serpentine domain walls move in response to a magnetic field H applied perpendicular to the sensor surface.	12
Figure 2.6: Idealized image and the actual image.	13
Figure 2.7: The step-down transformer arrangement and the current paths in the foil and test sample.	15
Figure 2.8: How a magneto-optic sensor must be modulated in order to obtain a useful magneto-optic image using the linear induction technique.	17
Figure 2.9: Waveforms for the eddy current excitation current and the bias coil. The waveforms are synchronized, and repeat about 26 times per second.	17
Figure 2.10: How the image of rivet is formed.	18
Figure 2.11: How the image is formed in the imager.	19
Figure 2.12: Quadrature Magnetic Yoke on a Pipe.	20
Figure 2.13: Images of Up-down Excitation (left) and Rotation Excitation (right).	21
Figure 5.1: (a) Original set A ; (b) disk structuring element; (c) dilation of A by B .	41
Figure 5.2: (a) Original set A ; (b) structuring element B ; (c) erosion of A by B .	42
Figure 5.3: The example of binary opening.	43
Figure 5.4: The example of binary closing.	44

Figure 5.5: The decomposition of structuring element.	46
Figure 5.6: (a) A gray-scale line; (b) various locations of a rolling ball during opening; (c) result of opening; (d) various locations of the rolling ball during closing; (e) result of closing.	50
Figure 6.1: Aluminum plate sample A with an EDM notch on it.	51
Figure 6.2: The image corresponding to the EDM notch in Figure 6.1.	51
Figure 6.3: Aluminum plate B with an EDM notch on it.	52
Figure 6.4: The image corresponding to the EDM notch in Figure 6.3.	52
Figure 6.5: Aluminum plate C with milled dome.	53
Figure 6.6: The image corresponding to milled dome in figure 6.5.	53
Figure 6.7: Aluminum plate D with milled dome.	54
Figure 6.8: The image corresponding to the milled dome in figure 6.7.	54
Figure 6.9: Layout of the obtained 6X6 images.	54
Figure 6.10: Images shifted and averaged in set B.	57
Figure 6.11: Images shifted and averaged in set A.	58
Figure 6.12: Images after morphological operations on set B images.	59
Figure 6.13: Image after 12 images in set B averaged and morphological operations.	59
Figure 6.14: Image after averaged and morphological operations in set B.	60
Figure 6.15: Image after averaged and morphological operations in set A.	60
Figure 6.16: Image after averaged and morphological operations in set A.	60
Figure 6.17: Image after correlation filtering and morphological operations in set D.	61

LIST OF TABLES

Table 2.1 The relation between frequency and penetration depth.	22
Table 3.1: Types of corrosion and their description.	25
Table 3.2: The types of aircraft alloys and the types of corrosion pervasive in that alloy.	26

ACKNOWLEDGEMENTS

I would like to express my sincere appreciation to my major professor Dr. William Lord for his guidance, encouragement and kindness during my graduate study.

I wish to sincerely thank to Dr. Satish Udpa, Dr. Lalita Udpa, Dr. Shiu Chi Han and Dr. Shridhar Nath. They gave me invaluable advice and help. I wish to thank to Dr. James Oliver for taking the time to serve on my thesis committee and his assistance.

I also would like to thank all the people in MCRG for your friendship and help.

I am always proud of my family's for your love, support and encouragement.

I also would like to thank NASA Langley Research Center for the financial support to undertake this research. In addition I appreciate the keen interest taken by Dr. Min Namkung and also for his encouragement and ideas. A special thanks to Mr. Thomas Heft of PRI, Inc. for providing the MOI images.

CHAPTER 1. INTRODUCTION AND NONDESTRUCTIVE TESTING METHODS

Introduction

Some fatigue cracks and corrosion (surface and subsurface) can lead to premature structural fatigue, failure and even severe disaster for both military and commercial aircraft, so reliable detection of them is an increasingly important issue. The existing predominant aircraft NDT techniques include visual inspection, eddy current inspection, X-ray, ultrasonics and dye penetrant [1]. Because small surface-breaking fatigue cracks about 0.1 inch long or shorter are typically covered by rivet heads and paint, only gross cracks can be found visually. While hand-scanned eddy current probe coils can detect small cracks near rivets, these techniques are time consuming and tedious. Moreover, because most conventional eddy current instruments display variations in the complex impedance seen by the probe coil (corrected for liftoff), flaw indications are ambiguous, so trained and experienced operators are needed to interpret results. In addition, liftoff variations produced by differences in paint thickness or surface roughness can cause false calls. False calls can result in expensive, unnecessary time consuming tear-downs and repairs. The use of the ultrasonic method for verification and quantification of corroded regions also is slow and tedious, requiring exact set up standards including accurate knowledge of substructures.

The existence of different types of corrosion, various structural thicknesses, presence of substructure and the reduction of resolution due to the use of lower frequencies for better depth of penetration, all contribute to the difficult task of reliably

detecting cracks and corrosion. These factors also contribute to the difficulty of developing well-defined standards for evaluating corrosion detection methods. Discussions with Boeing, McDonnell-Douglas and Lockheed NDT personnel indicate that the current requirement to qualify an instrument for performing inspections for hidden corrosion is to be able to reliably detect at least 10% loss of material on simulated lap skins [2]. Although higher sensitivity is desirable, no instrument has demonstrated the reliability to perform better. Furthermore, it is the aircraft manufacturer's opinion that manufacturing tolerances preclude accurate and reliable detection of corrosion loss or material thinning below approximately 5% [2].

Faster, simpler and more reliable inspection techniques are clearly needed to supplement or replace existing visual and eddy current methods. An acceptable, practical technique should have the speed and ease of interpretation of a visual inspection with the resolution of conventional eddy current inspections. The new magneto-optic/eddy current imaging technology appears to be capable of meeting the foregoing criteria by making it possible to obtain real time eddy current images of fatigue cracks and areas of corrosion in an airframe structure. Because the device employs an inductively coupled eddy current source, and because only magnetic fields are being sensed, there is no lift-off correction, so paint and other coatings need not be removed prior to inspections.

Methods of Nondestructive Testing

A variety of NDT methods have been used to address a large range of applications. Electromagnetic, ultrasonic, radiographic and microwave are mostly used

NDT methods. They differ from each other in the form of input energy used in interrogating the test sample.

Eddy Current Method

The eddy current method is based on the Maxwell-Ampere law and Faraday's law of electromagnetic induction. When a coil is excited by an alternating current, a time-varying magnetic field is generated. When a coil is moved close to a conductive sample, the time-varying magnetic field induces a current in the conductive sample. In accordance with Lenz's law, the induced eddy current will generate a magnetic field which opposes the field set up by the coil. Cracks and surface conditions modify the eddy current generated in the test sample, so the opposing magnetic field is altered. This leads to a change in the impedance of the coil. In practical eddy current measurements, a coil excited by sinusoidal current is placed above a conductive test sample and the impedance change of the coil is measured as the coil is moved over the test sample. We can detect and characterize defects by observing the change in impedance. Fig. 1.1 shows the method of eddy current NDT.

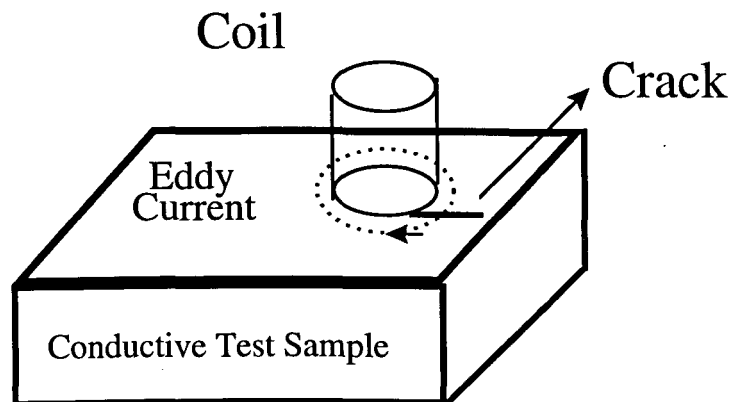


Figure 1.1 The method of eddy current NDT.

The impedance change of the coil is a complex value, which contains phase information. The phase is a function of flaw depth, by measuring the phase of the acquired data, we can differentiate near surface flaws and deep flaws.

Since the eddy current electromagnetic fields are diffusive fields, they only can penetrate for limited depth into the test sample. The penetration depth is dependent on the frequency f , the conductivity σ and permeability μ of the test sample as shown in the equation,

$$\delta = 1 / \sqrt{\pi f \mu \sigma} \quad (1.1)$$

For a particular sample, the conductivity and permeability are fixed, so we only can change the test frequency to control the penetration depth. The lower the test frequency, the deeper the penetration, the lower resolution.

The most used approach employs the magnetic flux leakage technique. The principle is that the flux leaks out to the surrounding area when there is a crack in a magnetized ferromagnetic test sample area. The leakage flux signal contains the information of the profile (shape and size) of the defect.

Multiple Test Frequencies and Data Fusion

As mentioned above, we can use higher frequencies to test near surface structures and lower frequencies to test deeper structures, so we can obtain better resolution for both near surface and deeper structures. If we use data fusion technique, combine the information for near surface structures with that for deeper structures, we can obtain an improved resolution which contains more information. Sun et al. [17,18] use the Q-transform to map the ultrasonic wave field to an equivalent diffusive field. The resulting

diffusive field is used to augment information obtained from eddy current NDE measurements. Song [19] describes a new morphological approach to fuse ultrasonic and eddy current NDE images.

In general, eddy current NDT images provide large contrast gray scale which shows the information of the depth of the defect. But at the same time, the large size of the probe compared to the width of the flaw results in severe blurring of the defect boundary.

Ultrasonic Test Method

Acoustic waves whose frequencies are above 20KHz are called ultrasonic waves [3]. The frequency range normally employed in ultrasonic NDT lies from 100KHz to 1GHZ [4]. When ultrasonic waves travel through the sample, they cause vibration or displacement of the particles in the sample. The test consists of sending a beam of sound into a test sample and examining the reflected or transmitted energy. The amplitude of the received signals and the time elapsed between the incident and the scattered signal (referred to as the time-of-flight (TOF)) are of interest in ultrasonic test [5]. For a given ultrasonic velocity, the time-of-flight data can be interpreted in terms of the location of the flaw whereas the signal amplitude can be related to the flaw size [6].

Generally speaking, there are three modes depending upon the manner in which data is displayed. The simplest A-scan signal is obtained by fixing the ultrasonic transducer position over the surface of the test sample and plotting the transducer response as a function of time, which indicates the flaw depth. A cross-sectional view of the flaw distribution can be obtained in B-scan, by moving the transducer linearly over

the surface of a sample under test and placing the A-scans next to each other to obtain an image. The C-scan image is an intensity mapping technique. By synchronizing the position of the spot on the oscilloscope screen with the transducer position, a plan view of the object is displayed by modulating the intensity of the spot by the amplitude of the signal at the receiving transducer [5].

For thin surface breaking cracks, ultrasonic images can provide very good resolution, highlighting the edges of the defect.

Radiographic Method

Radiographic methods use gamma rays or X-rays as the input energy source [7]. X-rays are a stream of high-energy electrons to be decelerated by the nuclei in the sample when the kinetic energy of the electrons is converted to electromagnetic radiation. Gamma rays are generated by transitions of radioactive nuclei from a high energy state to a more stable lower energy state. Since there is high energy content in this radiation, they can penetrate most materials. The intensity of the transmitted beam which is proportional to the thickness traversed by the beam is then recorded on a photographic film.

Microwave Method

Microwave can penetrate into dielectric media easily, the frequency and the loss factor of the dielectric material determine the depth of penetration. The phase and amplitude of the transmitted or reflected signal are used to analyze the test sample.

CHAPTER 2. MAGNETO-OPTIC/EDDY CURRENT IMAGER

Introduction and Background

As mentioned in chapter 1, the predominant existing aircraft NDE techniques include visual, eddy current, X-ray, ultrasonic and dye penetrant methods of inspections, each has advantages and disadvantages. The new magneto-optic/eddy current imaging technology promises to revolutionize the nondestructive inspection of aging aircraft and provide new methods to inspect materials such as nonmetallic composites. As the name implies, it is a combination of magneto-optic imaging techniques and novel eddy current excitation methods. By combining magneto-optic imaging and eddy current excitation in novel manner, it is possible to obtain real-time, eddy current images of fatigue cracks and areas of hidden corrosion in structures such as the fuselage of an aging aircraft. Recent improvements in this technology including multidirectional or rotating eddy current excitation by nonmechanical means, are discussed and illustrated in this chapter too.

Figure 2.1 shows the magneto-optic/eddy current imaging system. It consists of a power supply/control unit, an optional CCD TV camera and monitor, and a light weight, compact, hand-held imaging head [1].

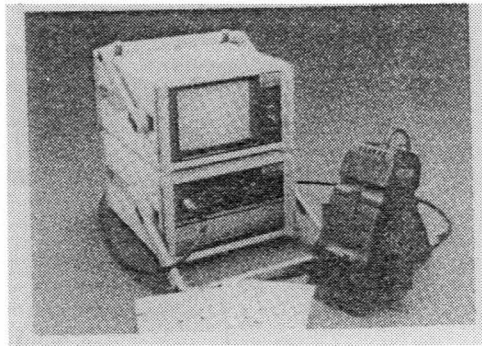


Figure 2.1 The Magneto-Optic/Eddy Current Imaging System [2].

Magneto-Optic and Eddy Current Technology

The magneto-optic/eddy current imager is a hybrid of magneto-optic sensing and eddy current induction. Two remarkable discoveries by Michael Faraday [8] in 1831 and 1845, namely Faraday's law of electromagnetic induction and the Faraday magneto-optic effect are the foundation for the new technology.

Faraday's law of electromagnetic induction states that a time varying magnetic field in the vicinity of an electrical conductor will induce a time varying electric field and thus a conduction current in the same conductor. We need to mention that the conventional techniques generally rely on currents flowing in coils to induce magnetic fields in the test sample, while the magneto-optic/eddy current technique induces the fields with current in a thin, planar foil placed near, and parallel to the surface of the test sample. This difference is illustrated in Figure 2.2. Conventional eddy current techniques rely on coils to induce magnetic fields, and to detect variations in the complex impedance due to defects. The magneto-optic/eddy current imaging method uses linear sheet induction technique to induce uniform electrical and magnetic fields parallel to the surface.

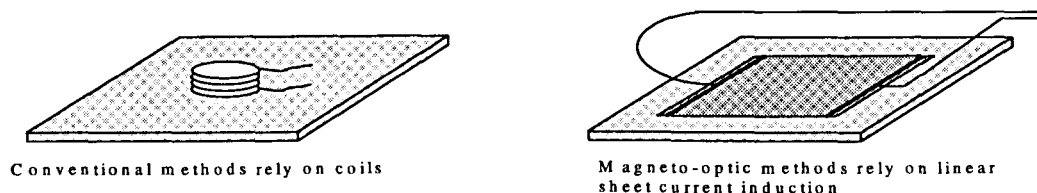


Figure 2.2 The comparison for induction methods between conventional eddy current technique and magneto-optic/eddy current imaging method [1].

In 1845 Michael Faraday observed that when plane polarized light was transmitted through glass in a direction parallel to an applied magnetic field, the plane of polarization of linearly polarized light was rotated. This is illustrated in Figure 2.3. Magnetic fields may affect the properties of material, particularly the optical properties. For the magneto-optic sensor, if normally incident, linearly polarized light is transmitted through such a magneto-optic sensor, the plane of polarization of the light will be rotated by an angle called the Faraday rotation θ , which is proportional to $\theta_f kM$, where k is the wave vector of the incident light (approximately perpendicular to sensor surface), and M is the local time dependent magnetization of the film at the point or region where light is transmitted [9]. M is generally directed, up or down, along the easy axis of magnetization. Because the angle between k and M completely determines the sign of the scalar product $k \cdot M$, the sense of the Faraday rotation for a given state of magnetization M does not depend on the sign of k , in other words, it does not depend on the direction the light is being propagated through the sensor. So the Faraday rotation will be doubled if the light is first transmitted through, and then reflected back through the sensor again, thereby enhancing sensitivity.

If we view this reflected light through an analyzer, as shown in Figure 2.4, the local state of magnetization of any region in the sensor can be seen as a high contrast dark or light area depending only on the direction of the magnetization M and the setting of the analyzer. This is the basic property that allows the sensor to create images of the normal-component magnetic fields of eddy currents.

One of the key requirements for a practical magneto-optic/eddy current imaging

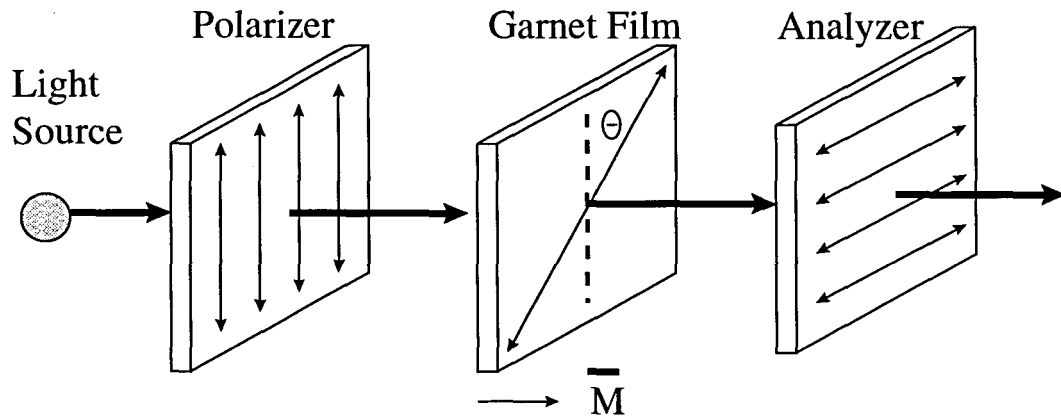


Figure 2.3 The Faraday Magneto-Optic effect.

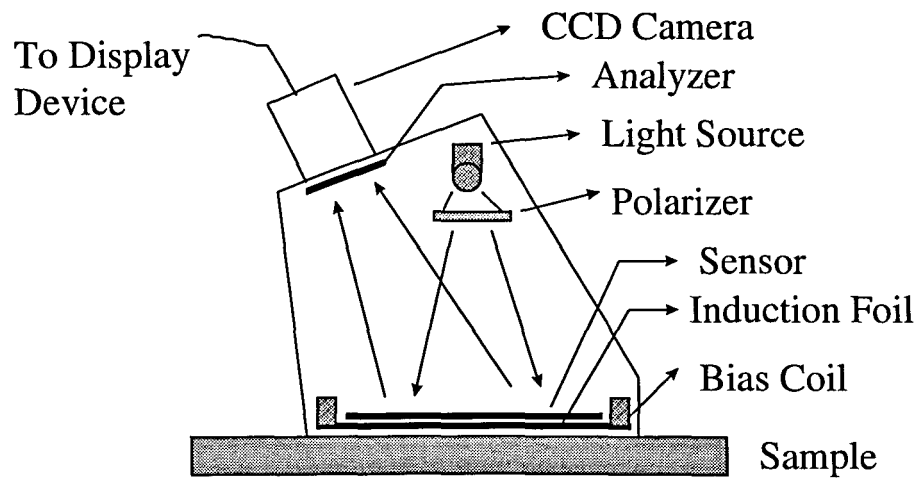


Figure 2.4 The Magneto-Optic/Eddy Current Imager uses a reflection mode geometry, this doubles the effective rotation angle.

system is the ability to induce uniform currents in a workpiece. Since the required induced currents are not circular but planar and linear in nature, we refer to them as sheet currents [1]. In a test sample such as aluminum, which is a good electrical conductor, the resultant eddy currents will be a significant fraction of the currents flowing in the foil, and can be made to flow uniformly.

Magneto-Optic Sensor

Components and Their Properties

Recently, the magneto-optic sensors consist of a thin film of bismuth-doped iron garnet $(Bi, Tm)_3(Fe, Ga)_5O_{12}$ grown on a 3-inch diameter, 0.020 inch thick substrate of gadolinium gallium garnet (GGG) [9,10,11]. These films have three physical properties that are essential for a practical magneto-optic/eddy current imaging device. First, they are magnetic anisotropic, that is, they have an easy axis of magnetization normal to the sensor surface and a hard axis of magnetization parallel to the sensor surface. Only normal component magnetic fields associated with cracks or corrosion, etc. will be detected by these sensors. Second, if the magnetic fields along the easy axis of magnetization are removed, the magneto-optic sensor will retain most of its established magnetization, that is, it has a memory. Third, because of the Bismuth doping, these films possess a relatively large specific Faraday rotation, up to 23,000 degrees/cm of thickness [12]. This means that even very thin garnet films (typically 3 microns) are capable of producing high contrast magneto-optic/eddy current images. We need to mention that the magnetic properties of garnets depend on their crystalline structure, chemical composition, and the presence of nucleation centers [13]. There may exist many different

types of magneto-optic garnets that could be used to sense the magnetic fields produced by eddy currents, so some or even significant improvements in the sensitivity and image producing characteristics of magneto-optic sensors are very likely to be achieved in the future.

Garnet Film Response

When a magnetic field is applied along the easy axis of magnetization of the sensor, domain walls associated with serpentine domains as shown in Figure 2.5, will begin to move at some threshold field (typically 1 to 3 gauss), thereby causing the domain to shrink or expand depending on the direction of the applied field [12]. If the applied magnetic fields are then turned off, the domain walls will generally be prevented from further motion by small nucleation centers present in the sensor [13]. This property insures that the sensors will remember these applied fields thereby making possible the imaging of time varying magnetic fields over a wide range of frequencies.

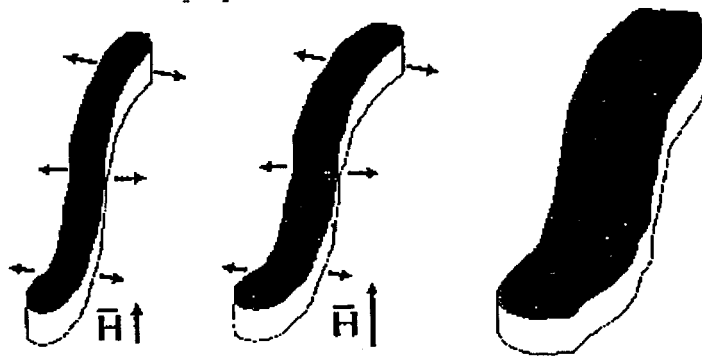


Figure 2.5 How the serpentine domain walls move in response to a magnetic field

H applied perpendicular to the sensor surface [12].

Since the basic properties of serpentine domains in applied external magnetic fields, we can understand how eddy current images can be formed using these sensors. By properly modulating the sensor, images of the type illustrated in Figure 2.6 can be produced by magnetic fields associated with the eddy currents. These fields are generally directed along the easy axis of magnetization thereby resulting in a real-time eddy current image of cracks or the corroded area.

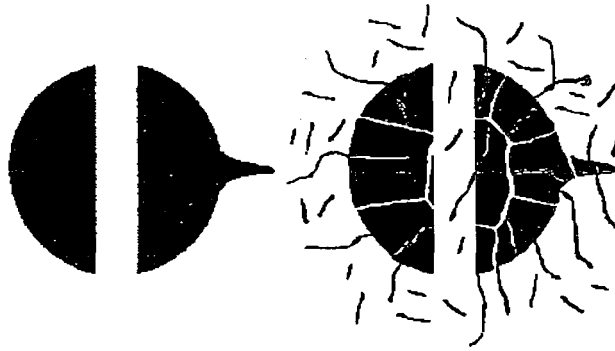


Figure 2.6 Idealized image and the actual image.

Sheet Current Excitation

Faraday's law of induction in differential form [14]

$$v = -N \frac{d\Phi}{dt} \quad (2.1)$$

$$\nabla \times \vec{E} = - \frac{\partial \vec{B}}{\partial t} \quad (2.2)$$

says that a time varying magnetic field B , in the vicinity of any electrical conductor will induce a time varying electric field E , and thus a time varying conduction current density $J = \sigma E$, in the same conductor. These source-free induced currents, by Lenz's law, are

always opposed in direction to the external currents which produce B . And the induced current density drops off exponentially from the surface of the conductor according to the rule $J = J_0 \exp(-x/\delta)$, where δ is the frequency and conductivity dependent skin depth of the conductor, x is the depth below the surface of the conductor.

Linear Sheet Current Excitation

As we mentioned above, the magneto-optic/eddy current imager using 3 inch diameter sensors must provide a means to excite uniform sheet-type eddy currents in the test sample. Fitzpatrick in [12] describes one of several possible step-down transformer arrangements that may be used to accomplish this task, as shown in Figure 2.7. The transformer consists of a primary winding on a ferrite, soft iron, or similar core material and a single turn secondary winding which includes a thin copper induction foil. The multiple turn primary of the transformer is connected to a relatively high voltage, low current source which is designed to deliver the appropriate voltages and currents at various frequencies currently ranging from 1.6 to 102.4 kHz [12].

It is possible to impose a very uniform potential difference across a single direction of the foil if we connect the secondary winding appropriately. The resultant currents in this foil induce current loops in the test sample which join in a common area to produce a region of uniform linear sheet current located just below the magneto-optic sensor.

Fitzpatrick [12] shows that the magnetic fields associated with such sheet currents generally lie parallel to the hard axis of magnetization of the sensor, which means that in

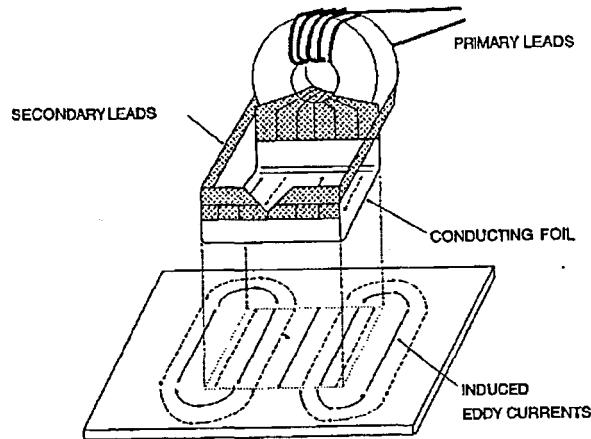


Figure 2.7 The step-down transformer arrangement and the current paths in the foil and test sample [12].

the absence of cracks or corrosion in the test sample, the magnetic fields exciting the eddy currents have little effect on the state of magnetization of the sensor, that is, they are not sensed. If this were not the case, these relatively large fields would completely overwhelm the much weaker fields produced by cracks and corrosion.

Magneto-Optic/Eddy Current Imaging

Fitzpatrick [12] illustrates schematically how the linear sheet-current excitation method is combined with the reflection mode magneto-optic imaging technique to produce a magneto-optic/eddy current image, as shown in Figure 2.8. For both the foil and the test sample the current paths are illustrated in this figure. In the first half cycle of a full current cycle, currents are indicated as solid lines, while currents in the second half cycle are indicated by dotted lines. Discontinuities in a test sample, such as a rivet or a crack can cause distortions in induced eddy currents, which produce detectable magnetic

fields normal to the surface of the test sample. These fields are the only fields detected by the sensor since it is only these magnetic fields which lie parallel to the sensor's easy axis of magnetization. These solid and dotted lines and curves in Figure 2.8 also show the normal component magnetic fields corresponding respectively to eddy currents induced in the test sample during the first and second half cycles of a given current cycle. Since these time varying magnetic fields can easily penetrate the thin (relative to a skin depth) copper foil at the frequencies the device generates, and they are generally associated with cracks or corrosion, so they are able to affect the state of magnetization of the sensor.

As shown in Figure 2.3, a relatively low frequency bias magnetic field is also applied to the magneto-optic sensor by a surrounding current-carrying coil, the resultant total magnetic field applied to the magneto-optic sensor, the modulation field, is the sum of these two fields and results in an image as shown in Figure 2.8.

Figure 2.9 shows the actual procedure in forming an image, where an additional erase pulse magnetic field, produced by a current flowing in the bias coil, is now included as part of the sensor modulation. First, the sensor is cleared of all images by the erase pulse and set to appear uniformly bright. Then a magnetic bias field from the bias coil, as indicated, along with the current in the foil are both established. During the time period alternating currents in the foil and the static bias fields are active, a sequence of images of the type shown in Figure 2.8 are produced. Finally, the sheet current excitation is turned off. Since the magneto-optic sensor has a memory, the images produced remain until the start of the next current generation cycle. Images are erased and refreshed about 26 times

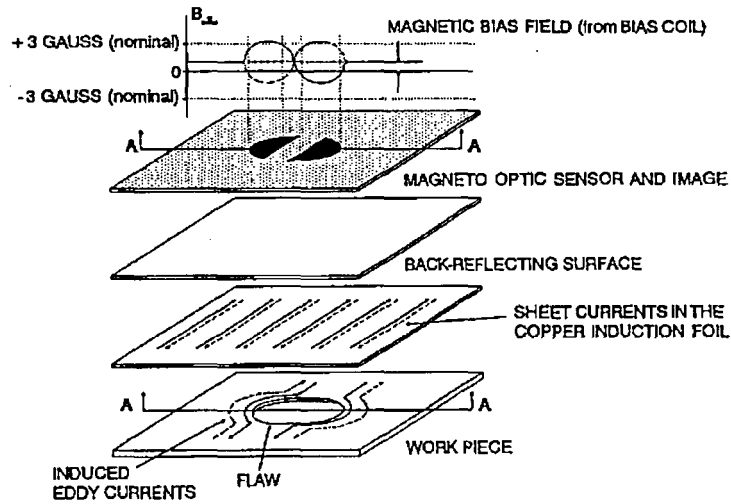


Figure 2.8 How a magneto-optic sensor must be modulated in order to obtain a useful magneto-optic image using the linear induction technique [12].

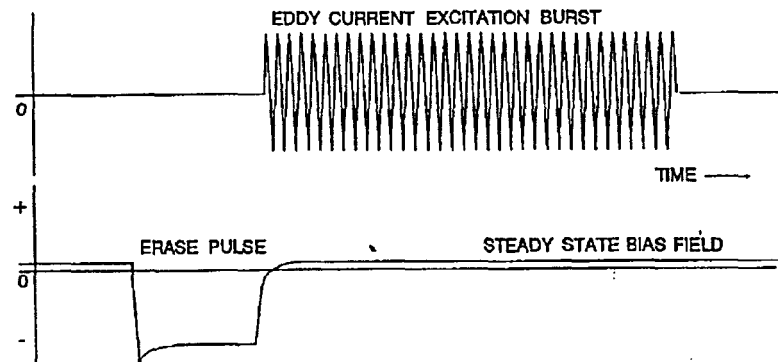


Figure 2.9 Waveforms for the eddy current excitation current and the bias coil.

The waveforms are synchronized, and repeat about 26 times per second [12].

per second [12].

The Forming of The Rivet Image

Figure 2.10 illustrates schematically how images of rivets are formed. In this figure, images are formed when defects or other obstructions such as rivets or holes divert the otherwise uniform flow of electric currents near the surface of the test sample. This creates magnetic fields perpendicular to the surface of the test sample which are readily imaged in real time by the magneto-optic/eddy current imager. Since alternating current is used to excite the workpiece, only half of the image is generated during each half cycle of applied current, as shown in the center sketches. This process occurs so rapidly, however, that the image appears to the inspector the whole image.

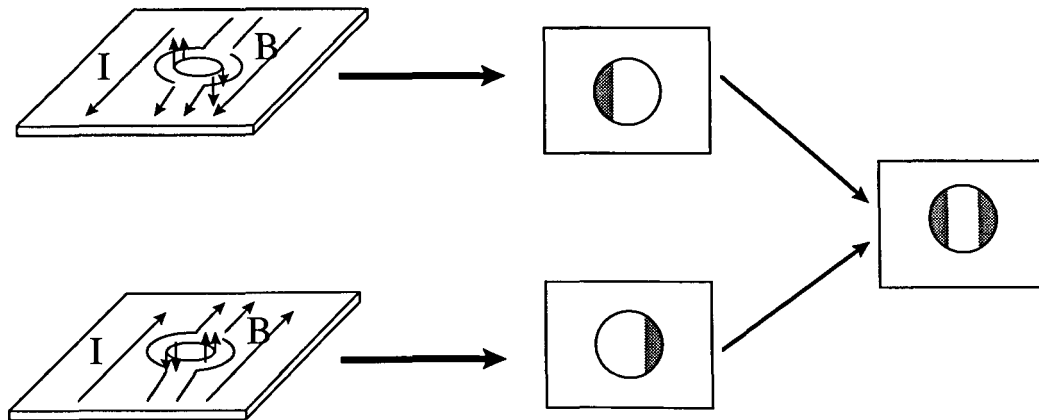


Figure 2.10 How the image of rivet is formed, I= Induced Eddy Current, B= Induced Magnetic Field [12].

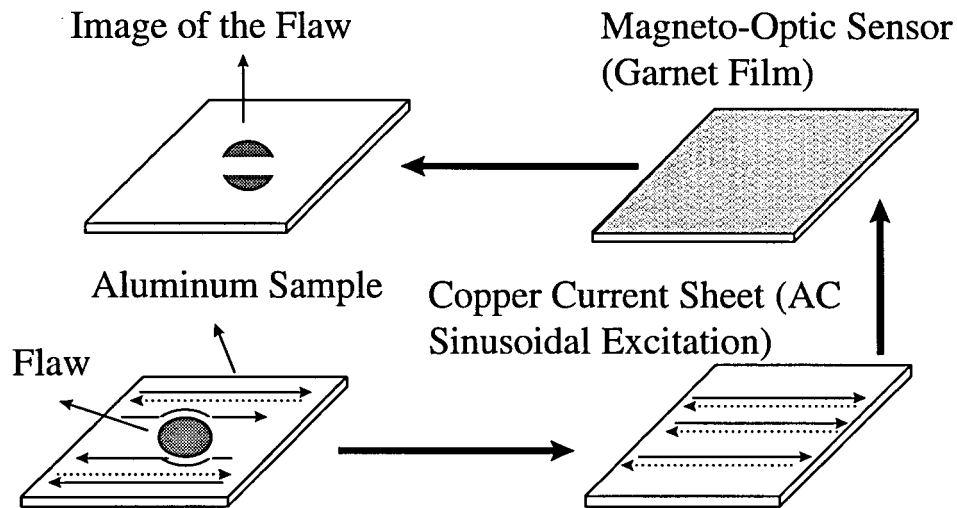


Figure 2.11 How the image is formed in the imager.

Improvement on MOI-Using Rotating Magnetic Fields

Background

One disadvantage of the introduced MOI is that it can not image cracks which are parallel to the direction of the linear magnetic current sheet, so we have to rotate the imager to image the cracks in all directions. To avoid this, multidirectional or rotating eddy current excitation by nonmechanical means are used. In practice, new developments in magneto-optic imaging have led to successful flux-leakage type imaging of cracks and/or corrosion in steel (e.g., plates, pipes or tanks) through insulation or protective coatings such as stainless steel cladding. The ROTOMAG system combines a magneto-optic imager of reduced size that nests inside a “quadrature magnetic yoke” cubicle producing rotating in-plane magnetization as shown in Figure 2.12. Not shown in the

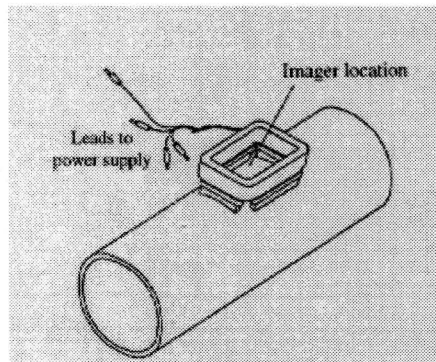


Figure 2.12 Quadrature magnetic yoke on a pipe [15].

drawing is a dual-channel power supply which drives the yoke coils (typically at 60 Hz).

Images are captured by a CCD camera located in the imager.

Multidirectional or Rotating Sheet Current Excitation

The idea is to use two separate primary coils (and cores), instead of using one as shown in Figure 2.7, electrically connected by two single turn secondary windings to a single foil [12]. The direction of currents from these two sources can be arranged to be perpendicular. In addition, two primary coils are excited with quadrature driving signals (sinusoidal waveforms 90 degrees out of phase) a multidirectional or rotating eddy current excitation of the test sample will be established. If we put a test sample under such a foil, there will be an induced current density at the surface of the form:

$$J = J_0 \sin(\omega t + \phi) \quad (2.3)$$

Two different in-plane vector current densities will exhibit a phase difference that depends only on the angle between them. Alternatively, by writing the current density J as

$$J = iJ_0 \sin(\omega t) + jJ_0 \cos(\omega t) \quad (2.4)$$

where i and j are orthogonal unit vectors, J can also be viewed as a linear sheet current density which rotates with an angular frequency ω . We called this as a multidirectional or rotating eddy current density.

Figure 2.13 shows MOI images of 0.5 inch-long EDM notches in a “cross” pattern in a flat A-36 steel plate. In a) only the “up-down” arm of the quadrature magnetic yoke was excited and in b) both arms of the yoke were excited (in quadrature) to produce rotating in-plane magnetization. Only half of the cross is visible in a) whereas the entire pattern is visible in b). In a word, crack orientation is not important when rotating magnetization is used.

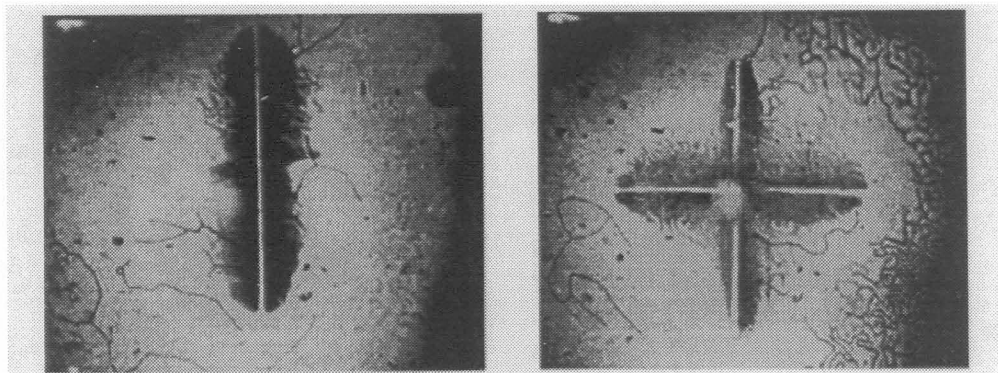


Figure 2.13 Images of Up-down Excitation (left) and Rotation Excitation (right) [15].

Frequency and Penetration Depth

The MOI is capable of inducing eddy currents in the frequency range from 1.6 to 102.4 KHz. At lower frequencies, it can detect and image subsurface cracking and corrosion in aluminum. At the higher frequencies, it can image and detect small, tight fatigue cracks near rivets near the outer surface of aluminum aircraft skins. From the MOI

Table 2.1 The relation between frequency and penetration depth.

FREQUENCIES (KHZ)	PENETRATION DEPTH (INCH)
1.6	0.120
3.2	0.084
6.4	0.060
12.8	0.043
25.6	0.030
51.2	0.021
102.4	0.015

operator's manual, Table 2.1 gives the relation between the frequency and the penetration depth.

The Advantages of MOI

W.C.L. Shih [1] showed that the MOI has generally met or exceeded some user's expectations, here is the summary of the advantages of the MOI:

1. Inspection Speed: 5-8 times faster than traditional methods.
2. Reliability: The MOI produces images of cracks that closely resemble the actual cracks, defects which are not near the surface may also be detected, provided that the eddy current skin depth is at least as great as the depth of the defect. Fatigue cracks as small as 0.02" measured from the edge of the rivet were detected and a very high probability of detection of cracks 0.05" and

larger was achieved. Technical improvements, such as multidirectional or rotating eddy current excitation and larger eddy currents, promise to enhance corrosion and sub-layer fatigue crack imaging capabilities.

3. Ease of Use: MOI is portable, light weight and hand-held, it is applicable to many different inspections requiring very little set-up time, the results can output to monitor, videotape or videoprinter, and the results are easy to interpret, so only minimal operator training is needed.
4. Paint and Decal: There is no need to remove the paint and decals, a major time and cost saving has been realized.

Imaging Processing Task on Images of MOI

The magnetic fields associated with small surface defects and subsurface defects are weak and more diffuse, so the defect indications get hidden by the magnetic domains and other noise. To improve the detectability of defects, an effective image enhancement method is needed, this is the main issue in this thesis.

CHAPTER 3. CORROSION TYPES AND ALLOYS IN AIRCRAFT

Introduction

Reliable detection of fatigue cracks and corrosion (surface and subsurface) is an increasing important issue for both commercial and military aircraft [2]. The understanding of types and nature of corrosion and types and nature of structure that are affected is useful to reach this goal.

Types and Nature of Corrosion

Shih in [2] describes the different types of corrosion that occur in aircraft. Each occurs at different points in the aircraft structure and is initiated in different ways. Table 3.1 shows the corrosion types and their description.

In [2], Shih also describes several types of aircraft alloys and shows the types of corrosion pervasive in that alloy, as shown in Table 3.2.

In many instances, the design of the aircraft can actually encourage corrosion development; galvanic corrosion typically occurs in aluminum skin joints with steel rivets, and pitting corrosion is almost inevitable in areas where moisture can collect [2].

Corrosion Detection Requirements

The existence of different types of corrosion, various structural thicknesses, presence of substructure and the reduction of resolution due to the use of lower eddy current frequencies for better depth of penetration, all contribute to the difficult task of reliably detecting hidden corrosion. Based on the aircraft manufactures recommendations, the ability to detect reliably a minimum of 10% loss of material due to corrosion would be necessary to qualify an instrument for corrosion inspection such as for lap splices [2].

Table 3.1 Types of corrosion and their description.

CORROSION TYPE	DESCRIPTION
Uniform chemical attack	the simplest and most common form of corrosion, this corrosion generally produces large area of damage.
Erosion	occurs in the presence of fast moving fluid, and has a rate of attack that is much faster than corrosion from still or slow moving sources. This corrosion is most common in propellers and turbine engine components.
Galvanic	metals of different electrochemical potential that are in contact cause galvanic corrosion. The corrosion occurs at the interface between two dissimilar metals.
Pitting	strongly localized attack produces pitting damage in the area of attack. Pitting is very common in metals with protective oxide films on them.
Crevice	occurs when a corrosive liquid gains access to crevices in, or between components. This situation occurs frequently in lap splices. It is very similar to pitting corrosion in many respects.
Intergranular& Exfoliation	occurs in the grain boundary regions in a polycrystalline metal. This can cause the grains to dislodge. Rolled or extruded metals with flattened grains can exhibit exfoliation, which is a severe form of intergranular corrosion.
Filiform	has characteristics of both pitting and intergranular corrosion. The corrosion is often found in clad aluminum alloys, where it an initial pit will penetrate the cladding, and then spread between the grains.
Fretting	vibratory motion between contacting surfaces can cause material loss due to both wear and corrosion. This type of loss can be serious, since fretting conditions can cause fatigue failures at very low stresses.
Microbiological	microbiological organisms can cause extensive corrosion in certain environments. The most common areas where biological corrosion occurs are in fuel tanks.
Stress Corrosion Cracking	components that are under sustained tensile stress in corrosive environments can experience this sort of corrosion damage.

Table 3.2 The types of aircraft alloys and the types of corrosion pervasive in that alloy.

ALLOYS	TYPE OF ATTACK TO WHICH ALLOY IS SUSCEPTIBLE
Aluminum Alloys	uniform, surface pitting, intergranular and exfoliation.
Titanium alloys	highly corrosion resistant. Extended or repeated contact with chlorinated solvents may result in degradation of the metals structural properties.
Magnesium alloys	highly susceptible to pitting.
Low alloy steels (4000-8000 series)	surface oxidation and pitting, surface and intergranular.
Corrosion Resistant Steel (300-400 series)	intergranular corrosion, some pitting in marine environments, stress corrosion cracking.
Nickel-base alloys (inconel)	sometimes susceptible to pitting.
Copper-base alloy, Brass, Bronze	surface and intergranular corrosion.
Chromium (wear-resistant plating for steels)	pitting in chloride environments.
Cadmium (as a protective coating for steel)	good corrosion resistance, will protect steel if attacked.

Detection of Hidden Corrosion With the MOI

To detect hidden corrosion, the existing techniques generally involve visual inspections followed by quantification using, for example, eddy current probes. These methods are not completely satisfactory due to the possibilities of either missing subtle hidden corroded regions or false indications. Use of existing eddy current and ultrasonic methods for verification and quantification of corroded regions is slow and tedious, requiring exact set up standards including accurate knowledge of substructures. The

Magneto-Optic/Eddy Current Imager (MOI), which uses magneto-optic principles to image eddy-current generated magnetic fields associated with surface and subsurface defects, can compensate for these limitations. MOI is capable of inducing eddy currents in the frequency range from 1.6 to 102.4 KHz. At the lower frequencies, the instrument can detect and image subsurface cracks and corrosion . At the higher frequencies, it can image and detect small, tight fatigue cracks around rivets on the outer surface of metallic aircraft skins through surface coverings such as paint or decals. This new visually-based inspection system has been approved by the major airframe manufactures and widely accepted for surface fatigue crack detection [2]. There is a very significant increase in inspection speed, more intuitive and easily interpreted inspection information, elimination of the need for paint and decal removal, virtual elimination of false calls, and ease of training providing sizable benefits to the industry. Even with the operational advantages, field tests have confirmed that the reliability and resolution of the MOI for surface fatigue crack detection as shown by probability of detection (POD) studies, is at least as good if not better than existing instruments [2].

CHAPTER 4. CORRELATION FILTERS FOR TEXTURE RECOGNITION

Introduction

The difficulty for texture recognition arises from the vast variations in texture information that are due to changing illumination, imaging conditions, thermal fluctuations, and even scale. Therefore it may be nearly impossible to devise a unique-recognition algorithm that is always successful. However, assuming favorable imaging and other necessary conditions, several texture recognition and segmentation algorithms have been proposed. These techniques rely on either simple operations such as thresholding, edge detection, region growing, and hierarchical schemes or more sophisticated approaches such as feature extraction, polygon fitting, smoothing, and probabilistic relaxation. Each of these approaches have respective merits and drawbacks depending on the type of imagery being processed and, in general, can be computation intensive.

Our interest is in designing correlation filters for texture recognition. A method that uses spatial filters for texture analysis has been discussed recently by Bovik [23, 24]. In this approach, spatial filters based on Gabor functions were shown to be useful for extracting orientation information and for establishing regions between different textures in an image. The authors adopted a multifilter (multichannel) approach to encompass a range of textured regions with different spatial frequency characteristics. The power of spatial filtering lies in the fact that several well-established algorithms and hardware exist for the two-dimensional convolution (or correlation) operation. If the spatial filters are

relatively small, multiple filters covering many textures can be implemented simultaneously in correlators without excessive demands on the space-bandwidth product. The simplicity of spatial filters may also be attractive for many real-time applications in which large images need to be processed in relatively little time and computationally intensive techniques based on segmentation are not an option.

The goal is to synthesize filters that can recognize particular textures in an image and that can highlight the corresponding regions. Thus our filters do not explicitly segment images, but they could make segmentation an easier task by greatly accentuating the pixel values in the regions of interest relative to elsewhere in the image. Much research has been done on correlation filters designed to recognize well-defined objects in the presence of distortion and noise. Synthetic discriminant functions and their variations optimize various performance criteria by use of multiple views of the objects as references. Certain approaches, based on circular-harmonic functions, attempt to lock on to rotation-invariant features. Other techniques use the phase of the image to satisfy the requirements of optical processors. The optimality of correlation filters has been investigated to evaluate the possible tradeoffs in their performances.

To date, much attention has been given to the use of correlation filters for the recognition of tangible shapes and objects. Mahalanobis [25] describes their use for recognizing another important type of pattern, namely, textures (terrains, surfaces, etc.), and ill-defined shapes. From a texture-recognition standpoint there are three interesting features of the proposed approach:

- Spatial filters avoid on-line statistical computations; statistical computations are used not for texture recognition, but for the off-line derivation of the masks that process texture information.
- The on-line computational simplicity makes the proposed approach suitable for real-time applications.
- The algorithm is geared for correlators (optical or digital); the filter size is fairly small so that many texture types can be accommodated in a single processor.

Another interesting issue is the detection process for the output of the filters. In conventional filters the correlation peak is used for this purpose. For the texture-recognition filters we propose, the detection criterion must be the output energy. All textures may have similar and significant energy at the input while at the output; the energy is expected to survive only in the texture of interest. A simple integrating or averaging process over the correlation plane can accomplish this.

Derivation of Spatial Filters for Texture Recognition

Mahalanobis [25] describes how to synthesize optimal filters that can discriminate between two different texture images, say, $x(m,n)$ and $y(m,n)$. We consider each image as a random texture of size $d \times d$ pixels, which is assumed stationary over some bounded region of interest. Both $x(m,n)$ and $y(m,n)$ are normalized to unit energy to eliminate overall intensity variations. Let $h(m,n)$ be the $l_1 \times l_2$ two-dimensional spatial filter.

The output of the filter in response to $x(m,n)$ is given by the 2-D correlation equation

$$g_x(m,n) = x(m,n)**h(m,n) = \sum_k \sum_l x(m+k,n+l)h(k,l) \quad (4.1)$$

where $**$ represents the 2-D correlation operation. Without loss of generality under the stationary assumption, and for simplicity, we consider behavior of the filter output at the origin, $g_x(0,0)$, with $m=0$ and $n=0$. For this point the correlation expression in Eq.(4.1) simplifies to

$$g_x(0,0) = \sum_k \sum_l x(k,l)h(k,l) \quad (4.2)$$

This can be expressed in vector notation as

$$g_x(0,0) = X^T h \quad (4.3)$$

where h and X are vectors of length $L=l_1l_2$ obtained by lexicographical reordering of the columns of $h(m,n)$ and a $l_1 \times l_2$ window of $x(m,n)$, respectively. This is the same as the standard expression for the output of synthetic-discriminant-function-type correlation filters used elsewhere.

Similarly the texture $y(m,n)$ produces $g_y(m,n)$ at the output of the filter, whose value at the origin is

$$g_y(0,0) = Y^T h \quad (4.4)$$

where Y is a vector of length L also obtained by lexicographical reordering of a $l_1 \times l_2$ window over a stationary region of $y(m,n)$.

Our aim is to find the filter $h(m,n)$ such that its output in response to $x(m,n)$ is strong [i.e., $g_x(m,n)$ appears as bright as possible], while its response to $y(m,n)$ is weak [and $g_y(m,n)$ is faint]. Such a filter would be useful for identifying all regions with texture similar to $x(m,n)$ while it suppresses other areas similar in texture to $y(m,n)$.

The brightness of each point in the filter output is determined by the energy at that point. Thus for highlighting a texture the corresponding points in the output should have maximum energy. Similarly if the texture is to be suppressed, the filter should minimize the energy in the output. The energy of $g_x(0,0)$ is given by

$$E_x = E\left\{\left[g_x(0,0)\right]^2\right\} = E\left[(X^T h)^2\right] = h^T E(XX^T)h = h^T R_x h \quad (4.5)$$

where $R_x = E(xx^T)$ is the $L \times L$ correlation matrix of $x(m,n)$ and E stands for the expectation. Similarly the energy of $g_y(m,n)$ is

$$E_y = E\left\{\left[g_y(0,0)\right]^2\right\} = E\left[(Y^T h)^2\right] = h^T E(YY^T)h = h^T R_y h \quad (4.6)$$

To maximize E_x while minimizing E_y , we maximize their ratio:

$$J(h) = \frac{E_x}{E_y} = \frac{h^T R_x h}{h^T R_y h} \quad (4.7)$$

The filter that maximizes $J(h)$ (also known as the Rayleigh quotient) will greatly amplify the energy of $x(m,n)$, making $g_x(m,n)$ bright while attenuating $y(m,n)$, thus making $g_y(m,n)$ faint. One can easily find the solution by taking the derivative of $J(h)$ with respect to h and by setting the gradient to zero. Specifically

$$\frac{\partial J(h)}{\partial h} = \frac{2R_x h}{h^T R_y h} - 2h^T R_x h \left[h^T R_y h \right]^{-2} R_y h = 0 \quad (4.8)$$

or

$$\frac{2}{h^T R_y h} \left(R_x h - \frac{h^T R_x h}{h^T R_y h} R_y h \right) = 0 \quad (4.9)$$

Let

$$\lambda = \frac{h^T R_x h}{h^T R_y h} \quad (4.10)$$

in Eq.(4.9) leads to

$$R_x h - \lambda \cdot R_y h = 0 \quad (4.11)$$

or

$$R_y^{-1} R_x h = \lambda \cdot h \quad (4.12)$$

The expression for λ in Eq. (4.10) is identical to $J(h)$, the function we are optimizing. From Eq.(4.12) we see that λ must be an eigenvalue of $R_y^{-1} R_x$ and that h is the corresponding eigenvector. Thus to maximize $J(h)$, we simply choose h to be the dominant eigenvector corresponding to the largest eigenvalue, λ_{max} , which is also the maximum value of $J(h)$.

A few comments regarding the solution are appropriate. As seen in Eq. (4.10), the eigenvalues λ represent the energy ratios [i.e., the actual value of $J(h)$] for the corresponding choice of eigenvector as the filter. Thus large eigenvalues represent more distinct separation of the textures. The inverse problem of recognition of texture $y(m,n)$ and suppression of texture $x(m,n)$ leads to the matrix $R_x^{-1} R_y$, whose eigenvalues are the reciprocals of those of $R_y^{-1} R_x$. The solution to the inverse problem is therefore found simply by selection of the weakest eigenvector corresponding to the smallest eigenvalue of $R_y^{-1} R_x$. In the frequency domain the filters are expected to form passbands at frequencies at which the texture to be recognized dominates, and to form stop bands elsewhere. The proposed algorithm does so in a statistically optimum manner based on the power spectrum of the data.

In principle, as implied by Eqs. (4.3) and (4.4), the filters optimize the performance measure with respect to the origins of the two correlation planes. However, regions of an image in which the texture remains the same (or similar) can be modeled as wide-sense stationary processes. Since the filters depend only on the second-order statistics, their behaviors remain the same even at points away from the origin, provided the statistics of these regions match the correlation matrices used to design the filters. Hence the filters amplify or attenuate arbitrarily wide regions in the image that resample the textures used in the training process.

Numerical Computation of the Filter

Given that h is the dominant eigenvector of $R_y^{-1}R_x$, the algorithm for its synthesis is as follows:

- (1) Estimate R_y and R_x from the sample texture images.
- (2) Compute $R_y^{-1}R_x$.
- (3) Find h , the dominant eigenvector of $R_y^{-1}R_x$.

The size of the filter should be chosen to be reasonably small for real-time application or for when the processor must include filters for several textures. The dimensions of the filter are related to its bandwidth. The smaller the filter, the larger its bandwidth and vice versa. The appropriate bandwidth for the filter (and hence its spatial dimensions) should be determined from the spectral characteristics of the texture and the spatial correlation between its pixels. For instance, if the pixels exhibit correlation over fairly large distances, then the spectrum of the texture is probably narrow, and a small bandwidth filter would suffice. Alternatively, if the pixels become uncorrelated rapidly,

then the texture probably has significant high-frequency content, which implies that the bandwidth of the filter should be large. The autocorrelation of the texture or its power spectral density can be used for making an educated choice for the filter size. However, for the purposes of discussing the theory and illustrating the optimization process we assume moderate correlation in the textures and arbitrarily choose filter sizes between 5×5 and 20×20 .

For practical choices of dimensions, steps (2) and (3) can be done on a modest computer. For instance, if $h(m,n)$ is a 10×10 mask, then h is a vector of length $L=100$ and the correlation matrices are of size 100×100 ; these can be handled without problems on existing computers. The main challenge lies in step (1) in estimation of R_x and R_y .

One method for estimating the $L \times L$ correlation matrix of a random image is to average the correlation matrices of all possible subimages of size $l_1 \times l_2$. If we define

$$w_i(m,n) = x(m+k_1, n+k_2),$$

$$0 \leq m \leq l_1 - 1, 0 \leq n \leq l_2 - 1 \quad (4.13)$$

as the i^{th} subimage starting at pixel location (k_1, k_2) , with $0 \leq k_1 \leq d-l_1-1$ and $0 \leq k_2 \leq d-l_2-1$, and with w_i as its vector representation of length L , then an estimate of the correlation matrix for $x(m,n)$ is

$$R_x = \frac{1}{P} \sum_{i=1}^P w_i w_i^T \quad (4.14)$$

where $P=(d-l_1+1)(d-l_2+1)$ is the number of possible subimages. However, this method is tedious and computationally unattractive for modest computers. Fortunately the same

matrix can be obtained efficiently from the autocorrelation function of the texture, defined as:

$$r_x(m, n) = x(m, n) ** x(m, n), \quad (4.15)$$

which can be rapidly computed by use of fast Fourier transforms on a digital computer. It can be shown that all elements of R_x are contained in the $(2l_1 - 1)(2l_2 - 2)$ region about the origin $r_x(0,0)$. The process of constructing R_x from $r_x(m, n)$ is best understood by means of an example. Consider a 2×2 subimage such as

$$w_i(m, n) = \begin{bmatrix} w_{0,0} & w_{0,1} \\ w_{1,0} & w_{1,1} \end{bmatrix} \quad (4.16)$$

The vector representation of $w_i(m, n)$ obtained by lexicographical reordering of its rows is

$$w_i(m, n) = \begin{bmatrix} w_{0,0} \\ w_{0,1} \\ w_{1,0} \\ w_{1,1} \end{bmatrix} \quad (4.17)$$

The correlation matrix is defined as the expectation of $w_i w_i^T$ and can be expressed in terms of the samples of the autocorrelation function $r_x(m, n)$ as

$$R_x = E(w_i w_i^T) \\ = E \left(\begin{bmatrix} w_{0,0} \\ w_{0,1} \\ w_{1,0} \\ w_{1,1} \end{bmatrix} \begin{bmatrix} w_{0,0} & w_{0,1} & w_{1,0} & w_{1,1} \end{bmatrix} \right)$$

$$= \begin{bmatrix} r_x(0,0) & r_x(0,1) & r_x(1,0) & r_x(1,1) \\ r_x(0,-1) & r_x(0,0) & r_x(1,-1) & r_x(1,0) \\ r_x(-1,0) & r_x(-1,1) & r_x(0,0) & r_x(0,1) \\ r_x(-1,-1) & r_x(-1,-0) & r_x(0,-1) & r_x(0,0) \end{bmatrix} \quad (4.18)$$

The elements of R_x can be identified as the samples of $r_x(m,n)$ whose indices are obtained by permutation of the subscripts on the elements of w_i and w_i^T in the corresponding row and column, respectively. Of course, $r_x(m,n)$ itself can be estimated in $d^2 \log(d)$ time from the sample texture images by use of fast Fourier transforms. After similarly estimating R_y , we obtain the dominant eigenvector solution for the filter by completing steps (2) and (3). We obtain the final mask by reshaping the eigenvector into an $l_1 \times l_2$ 2-D array of numbers.

In practice, if we want to keep the region of interest $x(m,n)$ and attenuate $y(m,n)$ ($x(m,n)$ and $y(m,n)$ are different), the algorithm can be modified as:

- (1) Estimate R_y from the sample texture images.
- (2) Compute R_y^{-1} .
- (3) Find h , the dominant eigenvector of R_y^{-1} .

CHAPTER 5. MATHEMATICAL MORPHOLOGY

Introduction

In Biology, the word morphology denotes the study of the form and structure of animals and plants [16]. The language of mathematical morphology is set theory [16]. Sets in mathematical morphology represent the shapes that are manifested on binary or gray scale images. For example, the set of all black pixels in a binary image is a complete description of the image. In image processing, we use the same word in the context of mathematical morphology as a tool for the analysis of geometric structure or texture within an image. The morphological approach to image processing is based on a primitive microstructure called structuring elements. The basic strategy employed in morphological image processing is to seek set-theoretical relationships between the given images and the predetermined structuring element by scanning the image using the structuring element. Appropriately used, mathematical morphological operations tend to simplify image data, preserving their essential shape characteristics and eliminating irrelevancies. Initially, morphological methods were applied to binary images. They were extended to analyze gray scale images later.

The primary morphological operations are dilation and erosion. From dilation and erosion the morphological operations of opening and closing can be composed. Opening and closing have a close connection to shape representation, decomposition and primitive extraction.

Binary Morphology

Basic Definitions

Let A and B be sets in Z^2 , with components $a=(a_1,a_2)$ and $b=(b_1,b_2)$, respectively.

The *translation* of A by $x=(x_1,x_2)$, denoted $(A)_x$, is defined as

$$(A)_x = \{c | c = a + x, \text{ for } a \in A\} \quad (5.1)$$

The *reflection* of B , denoted \hat{B} , is defined as

$$\hat{B} = \{x | x = -b, \text{ for } b \in B\} \quad (5.2)$$

The *complement* of set A is

$$A^c = \{x | x \notin A\} \quad (5.3)$$

The *difference* of two sets A and B , denoted $A-B$, is defined as

$$A-B = \{x | x \in A, x \notin B\} = A \cap B^c \quad (5.4)$$

Dilation

With A and B as sets in Z^2 and \emptyset denoting the empty set, the dilation of A by B , denoted $A \oplus B$, is defined as

$$A \oplus B = \left\{ x \left| \left(\hat{B} \right)_x \cap A \neq \emptyset \right. \right\} \quad (5.5)$$

so the dilation process consists of obtaining the reflection of B about its origin and then shifting this reflection by x . The dilation of A by B then is the set of all x displacements such that \hat{B} and A overlap by at least one nonzero element. Based on this interpretation, Eq. (5-5) can be rewritten as

$$A \oplus B = \{x | \left(\hat{B} \right)_x \cap A \subseteq A\} \quad (5.6)$$

Set B is referred to as the structuring element in dilation.

The dilation operation also can be represented as a union of translates of the structuring element: $A \oplus B = \bigcup_{a \in A} B_a$. This union can be thought of as a neighborhood operator. The structuring element B is swept over the image. Each time the origin of the structuring element B touches a binary-1 pixel, the entire translated structuring element shape is ORed to the output image where the initial output image has only zero-valued pixels. The final result is “fill”, “expand” or “grow”. Fig. 5.1 shows that (a) is the original set A , (b) is the disk like structuring element and (c) is the dilation of A by B .

Equation (5.5) is not the only definition of dilation in the current literature on morphology. But the preceding definition has a distinct advantage over other formulations in that it is more intuitive when the structuring element B is viewed as a convolution mask. Although dilation is based on set operations, whereas convolution is based on arithmetic operations, the basic process of “flipping” B about its origin and then successively displacing it so that it slides over set A is analogous to the convolution process.

Erosion

Erosion is the morphological dual of dilation. For sets A and B in Z^2 , the erosion of A by B , denoted $A \ominus B$, is defined as

$$A \ominus B = \{x | (B)_x \subseteq A\} \quad (5.7)$$

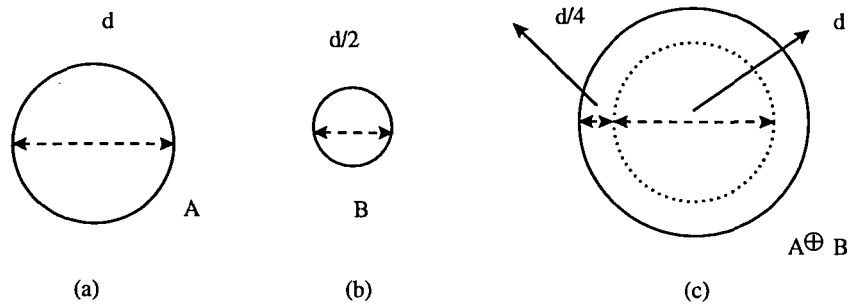


Figure 5.1 (a) Original set A ; (b) disk structuring element; (c) dilation of A by B .

which says that the erosion of A by B is the set of all points x such that B , translated by x , is contained in A . The structuring element B may be visualized as a probe that slides across the image A , testing the spatial nature of A at every point. Where B translated to x can be contained in A (by placing the origin of B at x), then x belongs to the $A \ominus B$.

Whereas dilation can be represented as a union of translates, erosion can be represented as an intersection of the negative translates:

$$A \ominus B = \bigcap_{b \in B} A_{-b} \quad (5.8)$$

Hence the same architecture that accomplishes dilation can be accomplished by erosion, changing the OR function to an AND function, and using the image translated by the negated points of the structuring element, instead of the image translated by points of the structuring element. In Figure 5.2, A is the original set, (b) is the structuring element and (c) is the erosion of A by B .

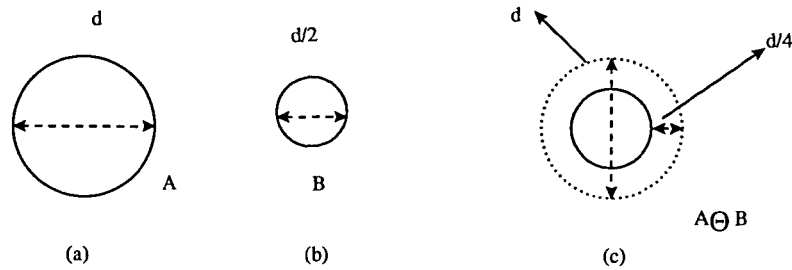


Figure 5.2 (a) Original set A ; (b) structuring element B ; (c) erosion of A by B .

As in the case of dilation, Eq. (5.7) is not only the definition of erosion. However, Eq. (5.7) is favored in practical implementations of morphology for the same reasons stated earlier.

Opening and Closing

As we have seen, erosion shrinks an image and dilation expands it. Dilation and erosion are usually employed in pairs, either dilation of an image followed by the erosion of the dilated result, or erosion of an image followed by the dilation of the eroded result, which are called closing and opening, respectively. In either case the result of successively applied dilations and erosions is an elimination of specific image detail smaller than the structuring element without the global geometric distortion of unsuppressed features. Opening generally smooths the contour of an image, breaks narrow isthmuses, and eliminates thin protrusions. Closing also tends to smooth sections of contours but, as opposed to opening, it generally fuses narrow breaks and long thin gulfs, eliminates small holes, and fills gaps in the contour.

Of particular significance is that image transformations employing successively applied dilations and erosions are idempotent, that is, their reapplication effects no further changes to the previously transformed result. The practical importance of idempotent transformations is that they comprise complete and closed stages of image analysis algorithms because shapes can be naturally described in terms of the structuring elements under which they can be opened or closed and yet remain the same.

The opening of set A by structuring element B , denoted $A \circ B$, is defined as

$$A \circ B = (A \ominus B) \oplus B \quad (5.9)$$

which says that the opening of A by B is simply the erosion of A by B , followed by a dilation of the result by B . In Figure 5.3, (a) is a disklike body and two elongated ellipselike handles; (b) is disklike structuring element with radius is just larger than the width of the larger ellipse and (c) is opening (a) with (b).

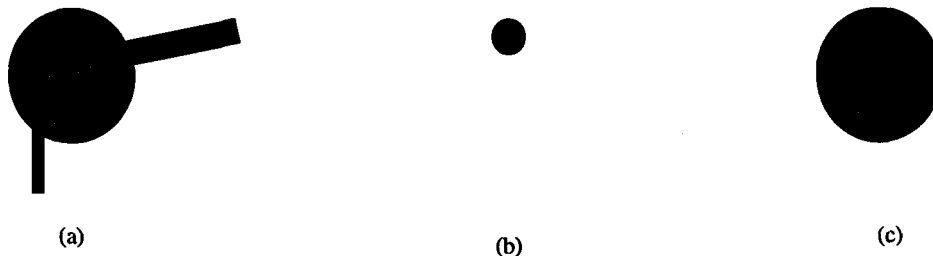


Figure 5.3 The example of binary opening.

The closing of set A by structuring element B , denoted $A \bullet B$, is defined as

$$A \bullet B = (A \oplus B) \ominus B \quad (5.10)$$

which says that the closing of A by B is simply the dilation of A by B , followed by the erosion of the result by B . Figure 5.4 (a) A binary image with five clusters of points.

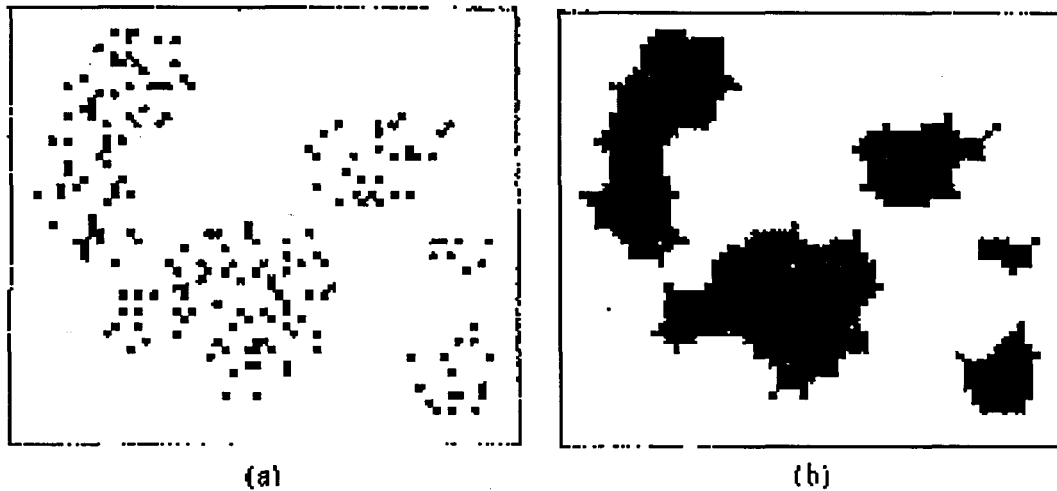


Figure 5.4 The example of binary closing.

Points within each cluster satisfy the partition property with distance ρ_0 , and the clusters are farther from each other than $2\rho_0$ pixels. (b) The image (a) closed by a disk with a radius just greater than $2\rho_0$.

Opening and closing have a simple geometric interpretation. Assume that we view the disk structuring element B as a flat “rolling ball”. The boundary of $A \circ B$ is then given by the points on the boundary of B that reach the farthest into the boundary of A as B is rolled around the inside of this boundary. In the other word, the points in the opening are precisely those obtained by sweeping the structuring element all over the inside of A , never permitting any part of the structuring element B to be outside A . This geometric fitting property of the opening operation leads to a set-theoretic formulation, which states that the opening of A by B is obtained by taking the union of all translates of B that fit into A . That is, opening can be expressed as a fitting process such that

$$A \circ B = \cup \{(B)_x \mid (B)_x \subset A\} \quad (5.11)$$

Closing has a similar geometric interpretation, except that now, again using the rolling ball example, we roll B on the outside of the boundary.

Structuring Elements

In morphological image processing, the image to be processed and the structuring element are an inseparable pair. Without specifying the structuring element, the description of a morphological operation is not complete.

Decomposition of Structuring Elements

We have never been content with the speed at which we accomplish any tasks. Fast computers, traffic tools and networks are required to save time. In image processing, we often need to process images in real time. Morphological routines can be time consuming depending on the size of the image processed and the size of the structuring element. For example, if we want to erode an image by a 3×3 structuring element, each pixel in the image generates 9 translates. But if it is eroded by a 20×20 structuring element, each pixel generates 400 translates. So there is a square increase in computational time with increase in the size of the structuring element.

Generally, the structuring element can be decomposed into a set of smaller sizes as shown by Serra [20,21,22]. Decomposition of structuring elements can be used to reduce computational time greatly. The theory underlying decomposition of structuring elements is given by the following theorem.

Theorem: If the structuring element B can be decomposed as: $B = B_1 \oplus B_2 \dots \oplus B_N$.

Then, the dilation and erosion of A by B can be performed as

$$A \oplus B = A \oplus (B_1 \oplus B_2 \dots \oplus B_N) = (((A \oplus B_1) \oplus B_2) \dots) \oplus B_N \quad (5.12)$$

$$A \ominus B = A \ominus (B_1 \oplus B_2 \dots \oplus B_N) = (((A \ominus B_1) \ominus B_2) \dots) \ominus B_N \quad (5.13)$$

The major problem in decomposing a structuring element is to determine the N smaller structuring elements. In figure 5.5, the larger structuring element can be decomposed into two small ones.

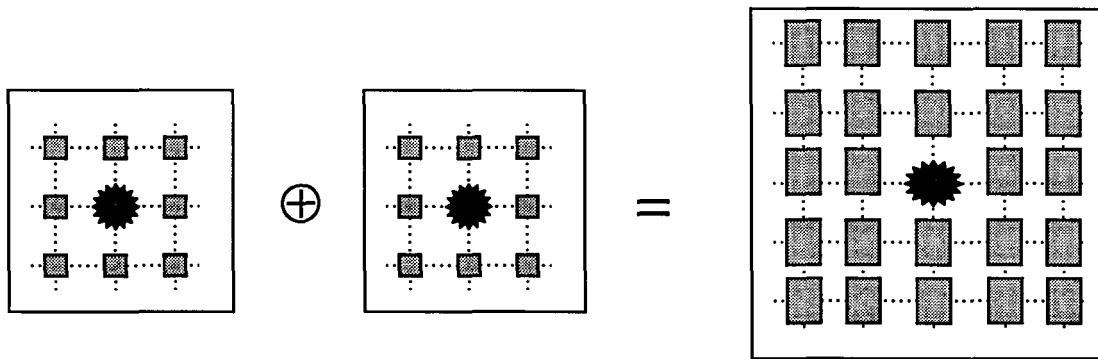


Figure 5.5 The decomposition of structuring element.

Gray Scale Morphology

Binary morphology has severe limitations. The growth of morphology as a discipline was handicapped by its incapability of handling multi-scale images. Images had to be thresholded into binary before applying morphological processing, which caused the original image to lose some information. This narrowed the spectrum of images on which morphology could be applied. Gray-scale morphology started taking shape in the late seventies and early eighties. The binary morphological operations are all naturally extended to gray-scale images by using neighborhood min and max operators.

The principles of mathematical morphology are applicable to sets in Euclidean or digital spaces without regard to their dimension.

Gray Scale Dilation

Assume that $f(x,y)$ and $b(x,y)$ are the input image and the structuring element, respectively. Usually, $b(x,y)$ is far less than $f(x,y)$.

Gray-scale dilation of f by b , denoted $f \oplus b$, is defined as

$$(f \oplus b)(s,t) = \max\{f(s-x, t-y) + b(x,y) \mid (s-x), (t-y) \in D_f; (x,y) \in D_b\} \quad (5.14)$$

where D_f and D_b are the domains of f and b , respectively. The condition that the displacement parameters $(s-x)$ and $(t-y)$ have to be contained in the domain of f is analogous to the condition in the binary definition of dilation, where the two sets had to overlap by at least one element. Note also that form of Eq. (5.14) is like that of 2-D convolution, with the max operation replacing the sums of convolution and the addition replacing the products of convolution.

Since dilation is based on choosing the maximum value of $f+b$ in a neighborhood defined by the shape of the structuring element, the general effect of performing dilation on a gray-scale image means: (1) if all the values of the structuring element are positive, the output image tends to be brighter than the input; and (2) dark details either are reduced or eliminated, depending on how their values and shapes relate to the structuring element used.

Gray Scale Erosion

Gray scale erosion, denoted $f \ominus b$, is defined as

$$(f \ominus b)(s, t) = \min\{f(s+x, t+y) - b(x, y) \mid (s+x), (t+y) \in D_f; (x, y) \in D_b\} \quad (5.15)$$

where D_f and D_b are the domains of f and b , respectively. The condition that the displacement parameters $(s+x)$ and $(t+y)$ have to be contained in the domain of f is analogous to the condition in the binary definition of erosion, where the structuring element had to be completely contained by the set being eroded. Note that the form of Eq. (5.15) is like that of 2-D correlation, with the min operation replacing the sums of correlation and the subtraction replacing the products of correlation.

Since dilation is based on choosing the minimum value of $f-b$ in a neighborhood defined by the shape of the structuring element, the general effect of performing erosion on a gray-scale image means: (1) if all the values of the structuring element are positive, the output image tends to be darker than the input; and (2) the effect of bright details in the input image that are smaller in “area” than the structuring element is reduced, with the degree of reduction being determined by the gray-level values surrounding the bright detail and by the shape and amplitude values of the structuring element itself.

Gray Scale Opening and Closing

The opening of f by b , denoted $f \circ b$, is

$$f \circ b = (f \ominus b) \oplus b \quad (5.16)$$

The closing of f by b , denoted $f \bullet b$, is defined as

$$f \bullet b = (f \oplus b) \ominus b \quad (5.17)$$

Opening and closing have a geometric interpretation, as shown in figure 5.6. Let b be a spherical structuring element here, then we view it as a “rolling ball”. The opening of f by b can be interpreted as the process of pushing the ball against the underside of the surface, while at the same time rolling it so that the entire underside of the surface is traversed, then the opening is the surface of the highest points reached by any part of the sphere as it slides over the entire undersurface off. All the peaks that were narrow with respect to the diameter of the ball were reduced in amplitude and sharpness. In applications, opening operations usually are applied to remove small (with respect to the size of the structuring element) light details, while leaving the overall gray levels and larger bright features relatively undisturbed. The initial erosion removes the small details, but it also darkens the image. The subsequent dilation again increases the brightness of the image without reintroducing the details removed by erosion. For closing, the ball slides on top of the surface, and peaks are left in their original form (so long as their separation at the narrowest point exceeds the diameter of the ball). In applications, closing is generally used to remove dark details, while leaving bright features relatively undisturbed. The initial dilation removes the dark details and brightens the image, and the subsequent erosion darkens the image without reintroducing the details removed by dilation.

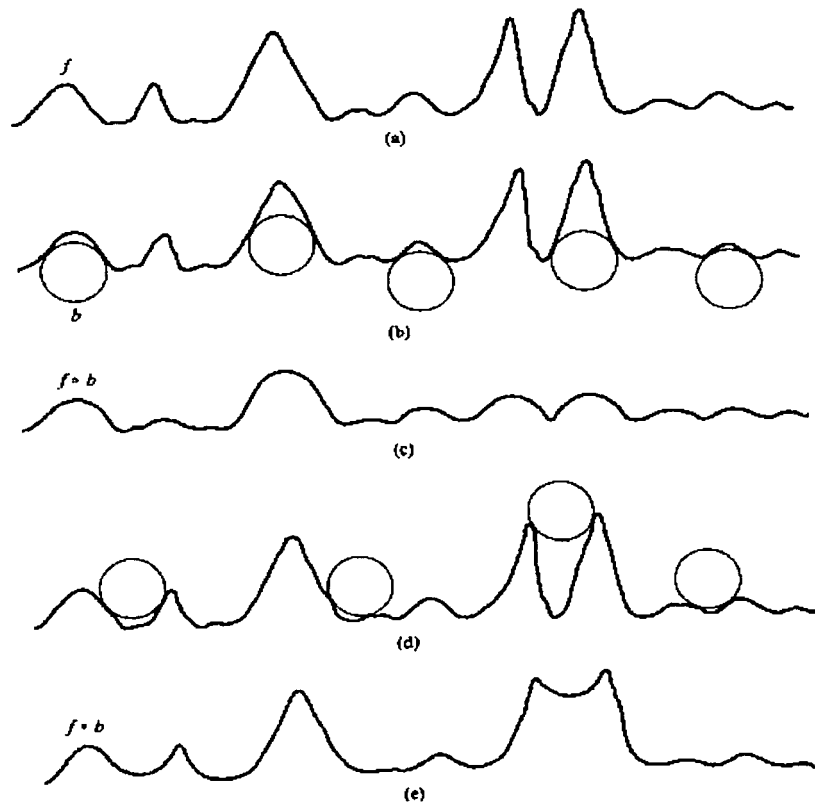


Figure 5.6 (a) A gray-scale line; (b) various locations of a rolling ball during opening; (c) result of opening; (d) various locations of the rolling ball during closing; (e) result of closing [16].

CHAPTER 6. RESULTS AND CONCLUSIONS

Introduction

In this chapter, we introduce the acquired MOI images and apply the methods introduced in Chapter 4 and Chapter 5 and averaging technique to these images.

Images and Layout

Four sets of images are presented and processed in this chapter. Figure 6.1 shows an aluminum plate A, with dimensions 6.25'' X 6.25'' X 0.059'' in length, width and thickness, respectively. There is an EDM notch on the aluminum plate whose dimension is 0.040'' X 0.001'' X 0.020''. Figure 6.2 shows one of the magneto-optic images corresponding to the EDM notch in Figure 6.1.

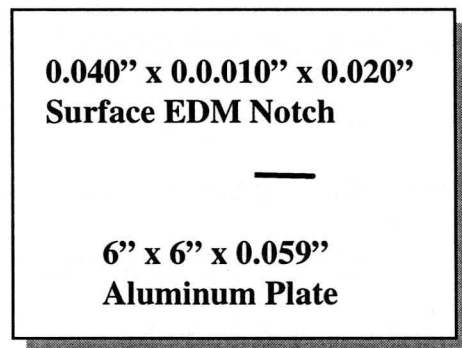


Figure 6.1 Aluminum plate sample A with an EDM notch on it.

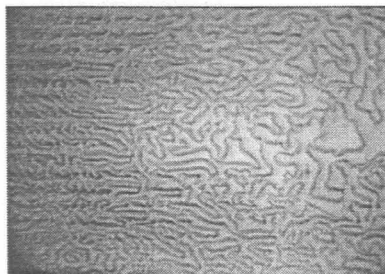


Figure 6.2 The image corresponding to the EDM notch in Figure 6.1.

Figure 6.3 shows an aluminum plate B, with dimensions 6.25'' X 6.25'' X 0.059'' in length, width and thickness, respectively. There is an EDM notch on the aluminum plate whose dimension is 0.120'' X 0.001'' X 0.040''. Figure 6.4 shows the image corresponding to the EDM notch in Figure 6.3.

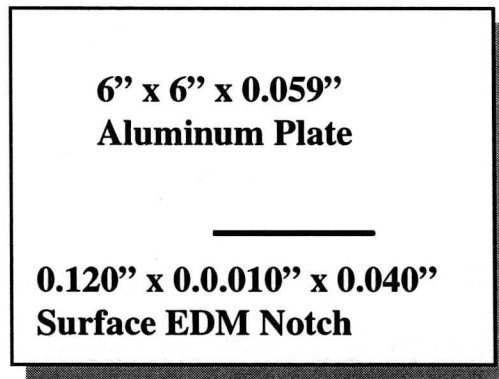


Figure 6.3 Aluminum plate B with an EDM notch on it.

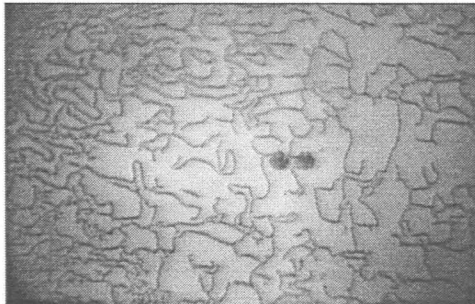


Figure 6.4 The image corresponding to the EDM notch in Figure 6.3.

Figure 6.5 shows an aluminum plate C, with dimensions 6.25'' X 6.25'' X 0.059'' in length, width and thickness, respectively. There is a milled dome on this aluminum plate with diameter 0.75'' and maximum depth 5% of the aluminum thickness. Figure 6.6 shows the image corresponding to the milled dome in Figure 6.5.

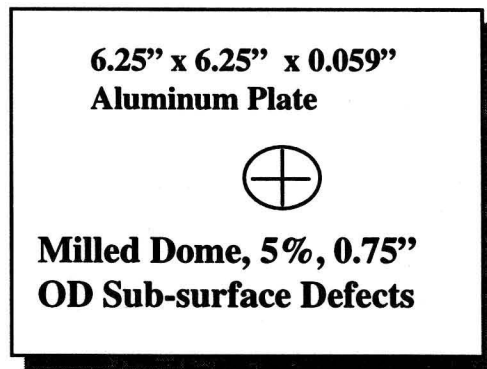


Figure 6.5 Aluminum plate C with milled dome.

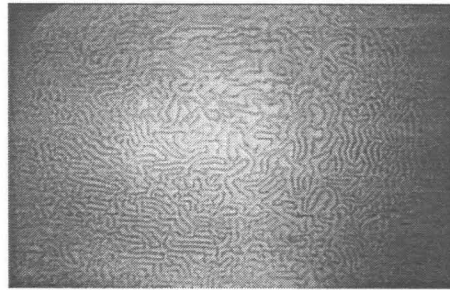


Figure 6.6 The image corresponding to milled dome in Figure 6.5.

Figure 6.7 shows an aluminum plate D, with dimensions 6.25'' X 6.25'' X 0.059'' in length, width and thickness, respectively. There is a milled dome on the aluminum plate with diameter 0.75'' and maximum depth 30% of the aluminum thickness. Figure 6.8 shows the image corresponding to milled dome in Figure 6.7.

Application of Correlation Filter, Averaging, Morphology

Correlation Filter

From the images of sets A and B, we can see that the textures of the background $x(m,n)$ and that of the defect $y(m,n)$ are different, our goal is to find the filter $h(m,n)$ such

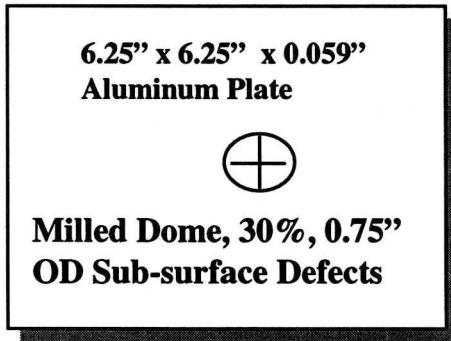


Figure 6.7 Aluminum plate D with milled dome.

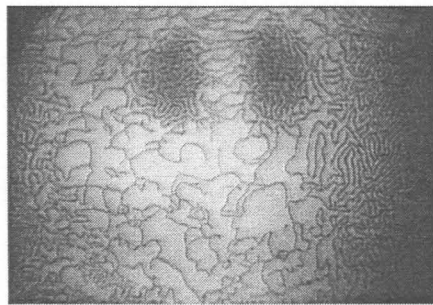


Figure 6.8 The image corresponding to the milled dome in Figure 6.7.

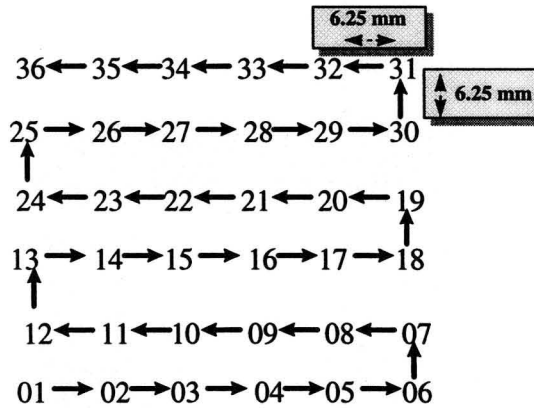


Figure 6.9 Layout of the obtained 6X6 images.

that its output in response to $x(m,n)$ is weak, while its response to $y(m,n)$ is strong. As discussed in Chapter 4, from $x(m,n)$ and $y(m,n)$, we estimate the auto-correlation matrix R_x and R_y , respectively, then filter $h(m,n)$ is the dominant eigenvector of $R_x^{-1}R_y$. If the input is $f(m,n)$, the output $g(m,n)$ is:

$$\begin{aligned} g(m,n) &= f(m,n) ** h(m,n) \\ &= \sum_k \sum_l f(m+k, n+l) h(k,l) \end{aligned} \quad (6.1)$$

Image Averaging

From the physics of the MOI phenomena, the background noise due to serpentine magnetic domains is highly correlated and can not be eliminated by averaging over multiple images taken at a single location. Therefore for each of the four cases, A, B, C, D, 36 images were generated by shifting the sensor by 0.25 inches in both directions. Figure 6.9 shows the sequence of the images taken to generate the data.

In each of the shifted images, the background serpentine magnetic domains of the sensor can be assumed to be uncorrelated with each other, so we can use large area averaging to suppress the background image i.e. to minimize the effect of the serpentine magnetic domains of the sensor.

Welch [26, 27] described that we average over K shifted images the best we can do is obtain a reduction of the variance by a factor 1/K of an original image, so averaging can significantly reduce the background texture noise.

The averaging is implemented here by choosing a reference image, shifting the other images correspondingly and then averaging them out. Although it was known that

the images obtained were shifted by 0.25 inch, it was difficult to determine the exact number of pixels needed to shift each image. The reason is that the actual image obtained at the camera level is trapezoidal, while the raw bitmap images given by PRI are rectangular. Experimentally, it was decided to shift the images in the horizontal direction by 85 pixels per inch, while those in the vertical direction were shifted by 66 pixels per inch.

Since set B imaged a larger flaw, the technique of shifting and averaging was applied to set B first. Figure 6.10 shows 12 images and 36 images shifted and averaged, respectively. This technique definitely shows that the background is suppressed or blurred out increasing the SNR of the image.

The same procedure is applied to set A to observe how well the technique performs. Figure 6.11 shows 12 images and 36 images shifted and averaged, respectively. We can see the defect which was not visible before performing averaging. We can conclude that large area averaging is the first step in a series of image processing techniques to enhance the corrosion image.

Morphological Operations

As introduced in Chapter 5, morphological operations are based on shape. Since defect and background texture have different shapes, we can perform morphological operations on these images. The appropriate choice of structuring element is the key to success of morphological operations.

Figure 6.12 shows the resulting images after gray scale morphological operations and binary morphological operations.

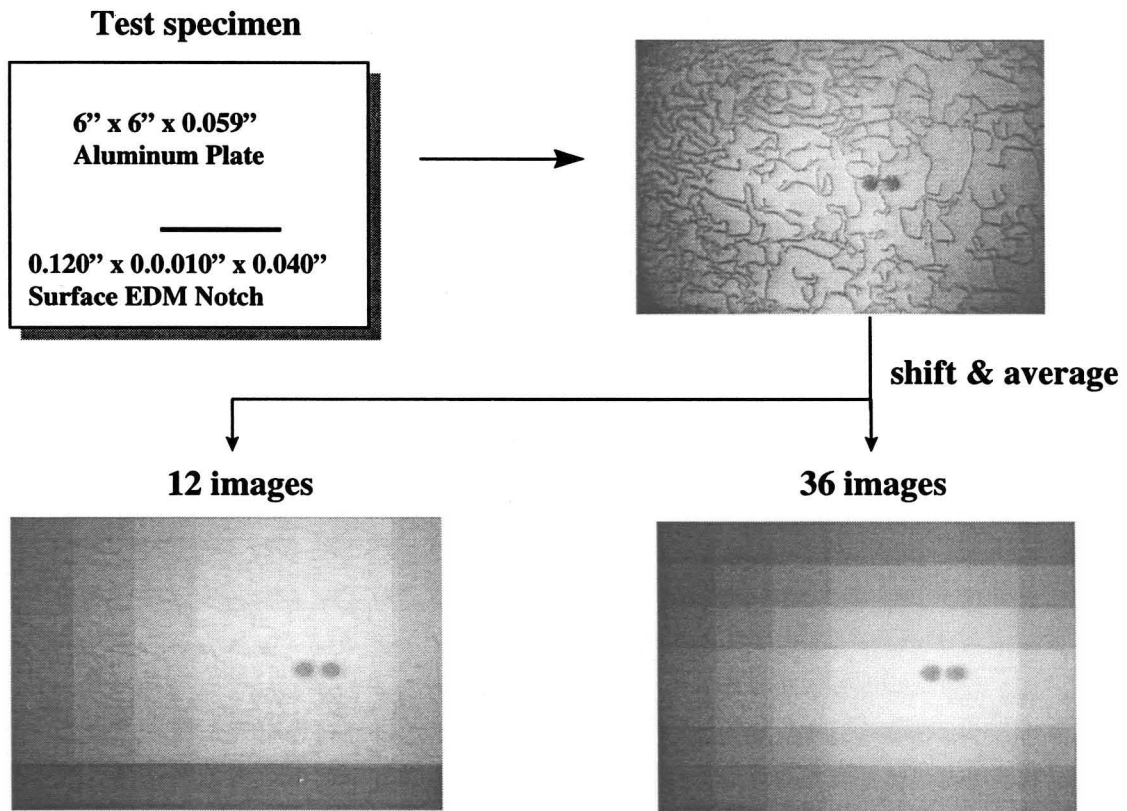


Figure 6.10 Images shifted and averaged in set B.

Averaging, Correlation Filter and Morphology Combined Operations

We have seen that using only one of these methods sometimes can not give a very satisfactory result for a small surface defect and weak subsurface defects, so combined methods are applied to these images.

Figure 6.13 shows results after 12 images are averaged and morphological operations performed in the zoomed area. The background of shifted and averaged image is greatly reduced, while the defect is enhanced. After performing morphological operations, only the defect is left and its shape is mostly kept.

Figure 6.14 shows results after all 36 images are averaged and morphological operations performed. The resulting image is better than that of Figure 6.13.

The same procedure is applied to set A to observe how well these techniques perform. Figure 6.15 shows the result after 12 images are shifted and averaged and morphological operations performed on that. We can see the defect which is not visible

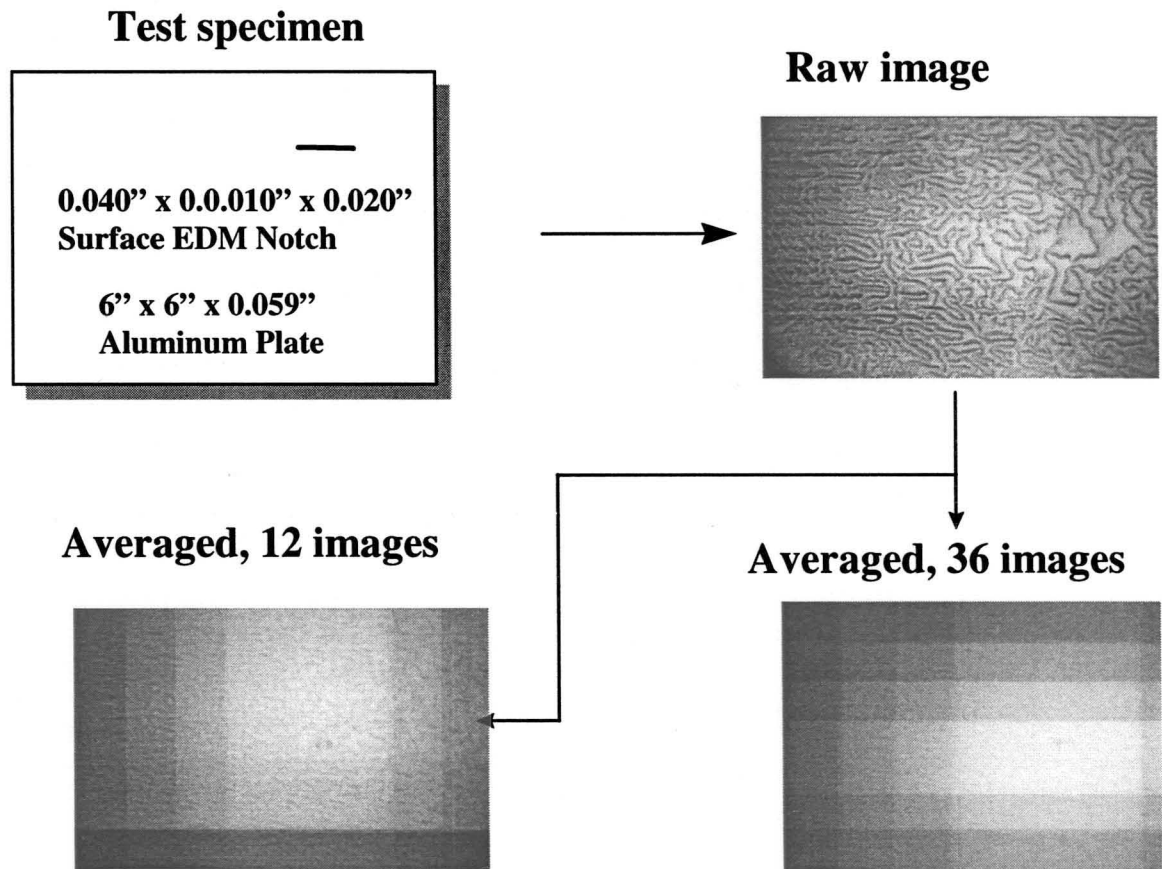


Figure 6.11 Images shifted and averaged in set A.

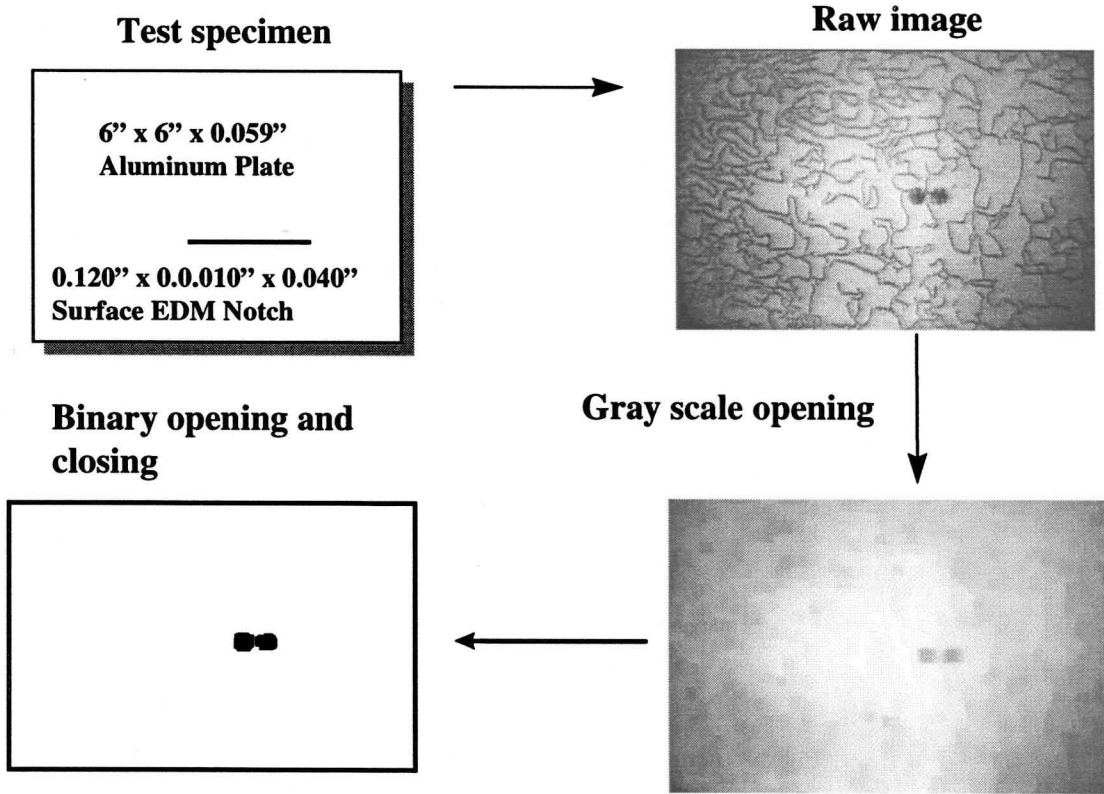


Figure 6.12 Images after morphological operations on set B images.

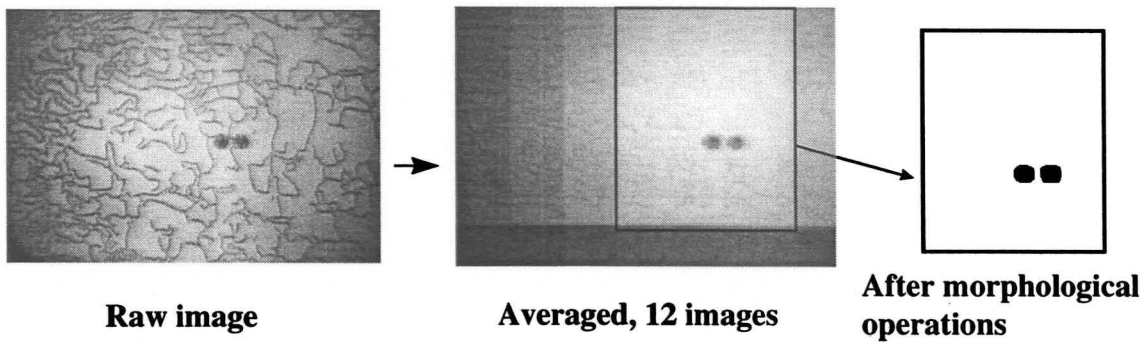


Figure 6.13 Image after 12 images in set B averaged and morphological operations.

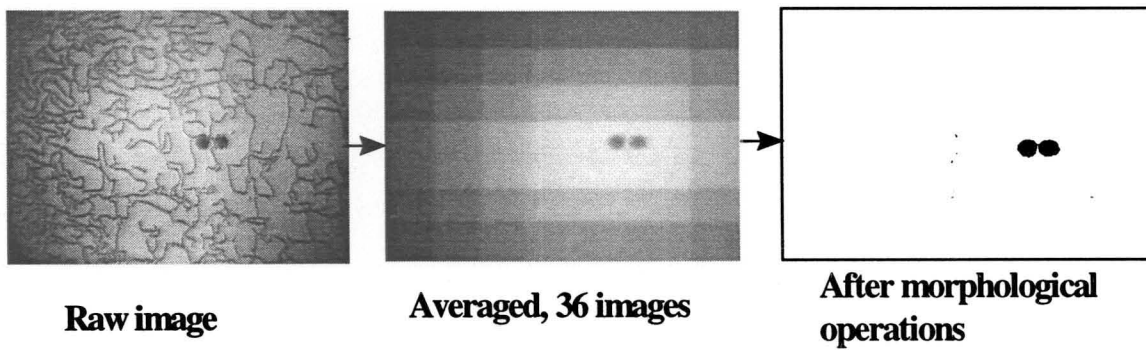


Figure 6.14 Image after averaged and morphological operations in set B.

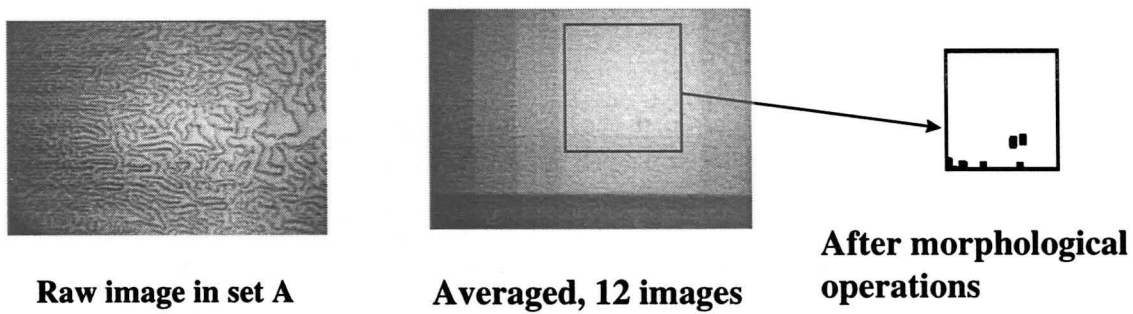


Figure 6.15 Image after averaged and morphological operations in set A.

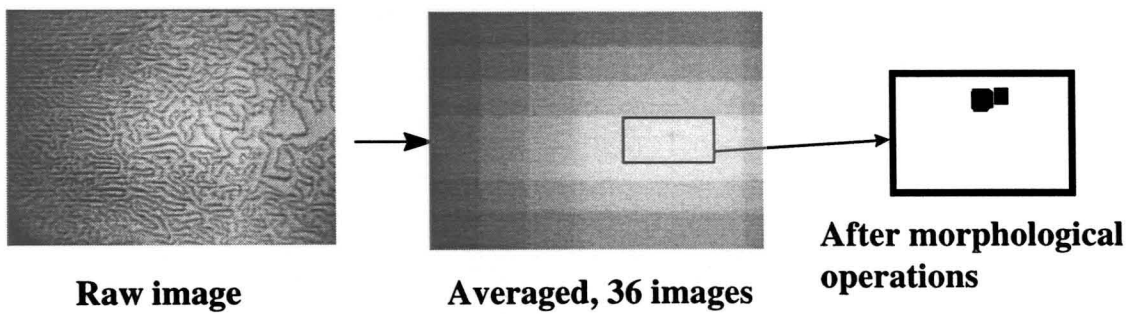


Figure 6.16 Image after averaged and morphological operations in set A.

before performing averaging and it is cleared after the morphological operations.

Figure 6.16 shows the image after 36 images shifted and averaged and morphological operations performed resulting in a better image than that of Figure 6.15.

Figure 6.17 shows the image after correlation filtering and morphological operations performed on that. After correlation filtering, the image has high contrast, then morphological operations were used to eliminate the background.

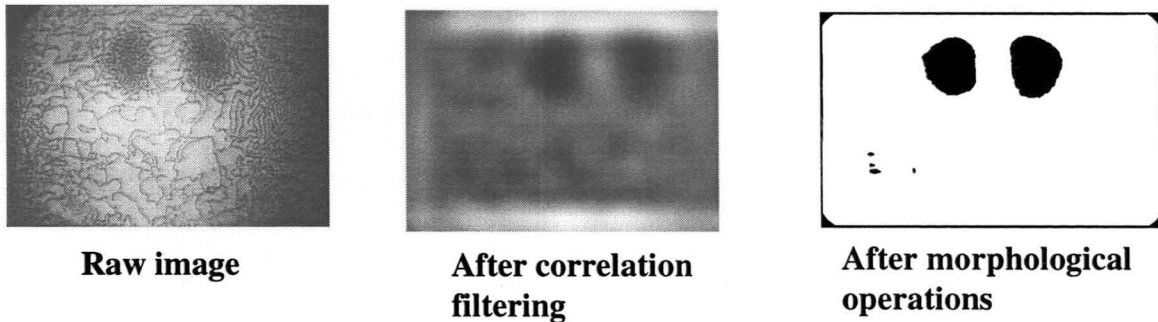


Figure 6.17 Image after correlation filtering and morphological operations in set D.

Conclusions

Averaging technique significantly decreases the background texture and increases the signal and noise ratio, it make the postprocessing task easier and efficient.

The correlation filter is a frequency-selective filter, the filter is expected to separate two textures provided the spectrum of one does not fully overlap with the other. The small filter size and the correlation-based design make it well suited for real time applications. The filter differentiate between textures by enhancing the energy in regions in which the specific texture occurs and by attenuating the image elsewhere. This

property of the filter makes it well suited for region labeling and for preprocessing for texture segmentation.

Morphological operations have successfully removed the background texture and highlighted the defect regions, so morphological image processing is an effective tool to enhance magneto-optic images. Since morphological operations are based on the shape of objects contained within the image, the characteristic of the image have to be known before processing. The structuring elements are the key for the morphological operations. When we choose an efficient structuring element, computation effort can be greatly reduced with little or no sacrifice of image quality. Since morphology is operator dependent, it is not suitable for automation.

Future Work

For correlation filtering, I will try to investigate the optional method to choose the filter dimensions and bandwidth based on the properties of the texture. The search for better structuring element should be continued to improve the resulting images. The decomposition of structuring element is also needed to save the computation time to satisfy the real time requirement. Since morphological operations are powerful tools, other applications of morphology are needed to be investigated. Other methods such as texture modeling and better image segmentation algorithms should also be deployed to images.

BIBLIOGRAPHY

1. W. C. L. Shih, G. L. Fitzpatrick, D. K. Thome, R. L. Skaugset, E. Y. C. Shih
"Aircraft Inspection with the Magneto-Optic/Eddy Current Imager," PRI
Instrumentation, Inc., Torrance, California, December 1992.
2. W. C. L. Shih, "Optimization of the Magneto-Optic/Eddy Current Imager (MOI) for
Detection of Subsurface Corrosion," Physical Research, Inc., Torrance, California,
1994.
3. J. Krautkramer and H. Krautkramer, *Ultrasonic Testing of Materials*, Springer-Verlag
Inc., New York, 1990.
4. R. B. Thompson and D. O. Thompson, "Ultrasonic in Nondestructive Evaluation,"
Proceedings of the IEEE, Vol. 73, No. 12, pp. 1716-1755, December 1985.
5. L. Udpa, *Imaging of Electromagnetic NDT Phenomena*, Ph.D. Dissertation, Colorado
State University, Fort Collins, Colorado, 1985.
6. J. Krautkramer, *Ultrasonic Testing of Materials*, Springer Verlag, Inc., New York,
1969.
7. R.C. McMaster, *Nondestructive Testing Handbook Vol. 1*, The American Society for
Nondestructive Testing, Columbus, Ohio.
8. R. M. Hutchins, "Great Books of the Western World," *Encyclopedia Britannica*, Vol.
45, 1992.
9. G. B. Scott, D. E. Locklison, "Magneto-Optic Properties and Applications of
Bismuth Substituted Iron Garnets," *IEEE Transactions on Magnetics*, MAG-12, July
1976.

10. A. H. Eschenfelder, *Magnetic Bubble Technology*, Springer-Verlag Inc., New York, 1980.
11. G. R. Pulliam, W. E. Ross et.al., "Large Stable Magnetic Domains," *Journal of Applied Physics*, Vol. 53, pp.2754, March 1982.
12. G. L. Fitzpatrick, D. K. Thome, R. L. Skaugset and E. Y. C. Shih, W. C. L. Shih, "Novel Eddy Current Field Modulation of Magneto-Optic Garnet Films for Real-Time Imaging of Fatigue Cracks and Hidden Corrosion," Physical Research, Inc., PRI Instrumentation Inc., Torrance, California, 1993.
13. J. A. Cape and G. W. Lehman, "Magnetic Domain Structures in Thin Uniaxial Plates with Perpendicular Easy Axis," *Journal of Applied Physics*, Vol. 42, No.13, pp. 5732-5756, December 1971.
14. M. N. O. Sadiku, *Elements of Electromagnetics*, Oxford University Press, New York, New York, pp. 412-413, 1995.
15. *Magneto-Optic/Eddy Current Imager Operator's Manual For Models 300 and 301*, PRI Instrumentation, Inc., Torrance, CA.
16. R. C. Gonzalez, Richard E. Woods, *Digital Image Processing*, Addison-Wesley Publishing Company, Inc., Reading, Massachusetts, pp.518, 1992.
17. K. Sun, *NDE Data Fusion Using Phenomenological Approaches*, Ph.D. Dissertation, Iowa State University, Ames, IA 1995.
18. K. Sun, S. Udpa, L. Udpa, T. Xue and W. Lord, "Registration Issues in the Fusion of Eddy Current and Ultrasound NDE Data Using Q-Transform," *Review of Progress in Quantitative Nondestructive Evaluation*, Vol. 15A, pp. 813-820, 1996.

19. Young-Won Song, *NDE Data Fusion Using Morphological Approaches*, Ph.D. Dissertation, Iowa State University, Ames, IA 1997.
20. X. Zhuang and R. M. Haralick, "Morphological Structuring Element Decomposition," *Computer, Vision, Graphics and Image Processing*, Vol. 35, No. 3. pp. 370-382, 1986.
21. O. I. Camps, T. Kanungo and R. M. Haralick, "Gray-Scale Structuring Element Decomposition," *IEEE Transactions on Image Processing*, Vol. 5, No. 1, pp. 111-120, January 1996.
22. J. Basart, M. S. Chackalackal and R. C. Gonzalez, "Introduction to Gray-Scale Morphology," In *Advances in Image Analysis*, Edited by Y. Mahdavih and R. C. Gonzalez, SPIE Optical Engineering Press, Bellingham, Washington, pp. 306-354, 1992.
23. A. C. Bovik, M. Clark, and W. S. Geisler, "Computational Texture Analysis Using Localized Spatial Filtering," *IEEE Computer Society Workshop on Computer Vision*, Miami Beach, Fla., December 1987.
24. A. C. Bovik, M. Clark, and W. S. Geisler, "Multichannel Texture Analysis Using Localized Spatial Filters," *IEEE Transactions on Pattern Analysis and Machine Intelligence*, Vol. 12, pp. 55-73, 1990.
25. A. Mahalanobis and H. Singh, "Application of Correlation Filters For Texture Recognition," *Applied Optics*, Vol. 33, No. 11, April 10, 1994.

26. P. D. Welch, "The Use Of The Fast Fourier Transform For The Estimation Of Power Spectra," *IEEE Transactions on Audio Electroacoustics*, Vol. AU-15, pp. 70-73, June 1967.
27. P. D. Welch, "A Fixed-Point Fast Fourier Transform Error Analysis," *IEEE Transactions on Audio Electroacoustics*, Vol. AU-17, pp. 153-157, June 1969.